

THE NORWEGIAN IPY-THORPEX

Polar Lows and Arctic Fronts during the 2008 Andøya Campaign

BY J. E. KRISTJÁNSSON, I. BARSTAD, T. ASPELIEN, I. FØRE, Ø. GODØY, Ø. HOV, E. IRVINE, T. IVERSEN,
E. KOLSTAD, T. E. NORDENG, H. MCINNES, R. RANDRIAMAMPIANINA, J. REUDER, Ø. SÆTRA,
M. SHAPIRO, T. SPENGLER, AND H. ÓLAFSSON

A field campaign out of northern Norway in winter 2008, including use of airborne lidar and targeted observations, provided new insight into the dynamics and predictability of polar lows and Arctic fronts.

Even today, more than 100 years after the Norwegian explorer Roald Amundsen first navigated the Northwest Passage, the Arctic remains a remote area with little human infrastructure. At the fringes of the Arctic Basin, where in winter the frigid Arctic air meets open waters, extreme weather in the form of poorly understood Arctic fronts and polar lows can develop. When the Arctic air masses move over the much warmer ocean, a large heat exchange between the ocean and the overlying air takes place, with the potential for the subsequent formation of convective weather systems. One of the hotbeds of such marine cold air outbreak (MCAO; Kolstad et al. 2009) activity is the northern North Atlantic, the Nordic Seas, and in particular the region between Svalbard and Norway.

Vilhelm Bjerknes, in a newspaper article in 1904, described the primary reason for the high frequency of severe weather over the Nordic Seas as follows:

“The northernmost part of Norway in winter is one of the stormiest locations on Earth, and the terrible accidents that occur from time to time, when large parts of the fishing fleet with crew and tools are lost, are only too well known. A look at the climatological conditions shows [that] the reason for the frequency of the storms [is that] the mean

temperature in January by the outermost Lofoten Islands is 27 degrees Celsius higher than the mean for the same latitude around the globe. This is the effect of the warm waters of the Gulf Stream. At the same time a Siberian winter cold reigns on the Finnmark plateau [in northern Norway]. Nature has, in other words, put an immense steam kettle side by side with an immense condenser. This steam engine must always work, and that is what it does, with great, irregular strokes.”

This study deals with three Arctic weather phenomena that can give rise to extreme weather that is often poorly predicted: polar lows (Rasmussen and Turner 2003), Arctic fronts (e.g., Grønås and Skeie 1999; Drüe and Heinemann 2001), and fierce low-level winds generated by flow over and around orography in stably stratified conditions (e.g., Skeie and Grønås 2000; Renfrew et al. 2009). In general, NWP errors tend to be larger in the Arctic than at midlatitudes (Nordeng et al. 2007), for the following reasons:

- First, the conventional observational data network in the Arctic is sparse. Satellites are therefore crucial in filling the observational gaps, but despite the excellent temporal coverage by polar-orbiting satellites, they are not yet able to compensate for

the lack of radiosonde data. Nevertheless, the value of satellite observations for NWP, for example through the Advanced Microwave Sounding Unit (AMSU-A) and the Infrared Atmospheric Sounding Interferometer (IASI), has been demonstrated by several investigators (e.g., Cardinali 2009; Hilton et al. 2009).

- Second, the weather phenomena listed in the previous paragraph are poorly represented in current numerical weather prediction models. This deficiency is partly due to the small spatial scales needed to resolve the processes responsible for severe weather phenomena (e.g., polar lows are an order of magnitude smaller than synoptic-scale cyclones). In addition, moist convection, which is a major challenge for NWP models (Yano and Geleyn 2010), is an important component in polar low development (Rasmussen and Turner 2003). Furthermore, the NWP models are known to have large biases in their treatment of the Arctic planetary boundary layer (Tjernström et al. 2005). These biases can significantly degrade the ability to simulate the phenomena in question.

Polar lows and other weather phenomena associated with MCAOs are treacherous in that they often arrive from the north during otherwise calm weather. In the television documentary about the International Polar Year (IPY)–The Observing System Research and Predictability Experiment (THORPEX) flight campaign, a fisherman from northern Norway explained how he and his brother saw a wall of dark

clouds approaching from the north when they were surprised by a poorly forecasted polar low. Their boat capsized and his brother drowned. According to the former director of the weather forecasting office in Tromsø, Kari Wilhelmsen (in Grønås and Skeie 1999), 56 vessels were lost at sea and 342 people died in Norwegian waters during the twentieth century. Undoubtedly a fair share of these deaths were due to weather associated with MCAOs, because these phenomena hit more abruptly with less warning in the form of classical weather signs than synoptic-scale cyclones.

Detailed in situ measurements of atmospheric characteristics in polar lows by research aircraft are rare. The very first flight of this kind took place on 27 February 1984 during the Norwegian Polar Low Project, when the National Oceanic and Atmospheric Administration (NOAA) WP-3D research aircraft penetrated an intense polar low over the Norwegian Sea southeast of Jan Mayen (Shapiro et al. 1987). Surface fluxes of sensible and latent heat were both estimated at about 500 W m^{-2} (Shapiro et al. 1987). However, it is important to note that those estimates were based on flights at 300 m above the surface and therefore cannot be regarded as direct measurements. The observations revealed a warm, moist inner core all the way up to 580 hPa and maximum wind speeds up to 35 m s^{-1} at two locations near the center of the polar low. Subsequent NWP model simulations (Grønås et al. 1987) showed that the model significantly underestimated the strength of the polar low, even though the initial conditions from the European Centre for Medium-Range Weather Forecasts (ECMWF) analysis appeared surprisingly realistic. The next two polar low flights were carried out over the northern Gulf of Alaska during the 1987 Alaska Storms Program (Douglas et al. 1991). A polar low was penetrated on two consecutive days (2–3 March 1987) with the NOAA WP-3D, revealing a gradual deepening of the low and an increase of the vertical extent of the circulation with time. Similar to the polar low near Jan Mayen, the Alaskan polar low developed a warm core, even though it developed in a baroclinic environment. Returning to the Norwegian Sea with the NOAA WP-3D, the structure of a polar low near Greenland was investigated during the Coordinated Eastern Arctic Experiment (CEAREX) 1989 campaign (Douglas et al. 1995). This rather weak system had most of its circulation below 800 hPa. Nevertheless, an upper-level vorticity perturbation was also found, suggesting a possible coupling between low-level and upper-level baroclinicities, as suggested in a previous theoreti-

AFFILIATIONS: KRISTJÁNSSON, FØRE, AND McINNES—University of Oslo, Oslo, Norway; BARSTAD AND KOLSTAD—Uni Bjerknes Centre, Bergen, Norway; ASPELIEN, GODØY, HOV, IVERSEN, NORDENG, RANDRIAMAMPIANINA, AND SAETRA—Norwegian Meteorological Institute, Oslo, Norway; IRVINE—University of Reading, Reading, United Kingdom; REUDER, SHAPIRO, SPENGLER, AND ÓLAFSSON—Geophysical Institute, University of Bergen, Bergen, Norway

ADDITIONAL AFFILIATIONS: SHAPIRO—NCAR, Boulder, Colorado; SPENGLER—Princeton University, New Jersey; ÓLAFSSON—University of Iceland, and Icelandic Meteorological Service, Reykjavík, Iceland

CORRESPONDING AUTHOR: J. E. Kristjánsson, Department of Geosciences, MetOs, University of Oslo, P.O. Box 1022, Blindern, N-0315 Oslo, Norway

E-mail: j.e.kristjansson@geo.uio.no

The abstract for this article can be found in this issue, following the table of contents.

DOI:10.1175/2011BAMS2901.1

In final form 7 June 2011
©2011 American Meteorological Society

cal paper by Montgomery and Farrell (1992) and in a numerical study by Grønås and Kvamstø (1995). It was not until the 2005 Lofoten Cyclone campaign (LOFZY; Brümmer et al. 2009) that low-level flights (less than 50 m above the surface) were carried out in a polar low environment, thereby allowing direct measurements of surface fluxes of sensible and latent heat using high-frequency (100 Hz) sampling of vertical velocity, temperature, and specific humidity. In the flight on 7 March 2005, areal averages of sensible and latent heat of 115 and 190 W m^{-2} , respectively, were obtained in a shallow and short-lived polar low over the Barents Sea between Norway and Svalbard. The highest fluxes of 290 and 520 W m^{-2} , respectively, were found underneath a cloud band to the north of the polar low center.

In summary, these observational studies indicate that a complex interplay among low-level baroclinicity, upper-level forcing, sensible and latent heat fluxes, and latent heat release contributes to polar low genesis and intensification. This interplay has been addressed by theoretical and modeling studies: Some of them have merely focused on the moist convection associated with polar lows and have used hurricane theory to explain polar low evolution. Rasmussen (1979, 1981) suggested conditional instability of the second kind (CISK) as a crucial mechanism in organizing the convection, and in support of this (Rasmussen et al. 2003) seemingly found evidence of a reservoir of convective available potential energy (CAPE) over the Norwegian Sea in polar low situations. Emanuel and Rotunno (1989) coined the term “arctic hurricanes” for polar lows, and proposed wind-induced surface heat exchange (WISHE) as the mechanism for their development. Other studies (e.g., Mansfield 1974; Duncan 1977) have focused on the baroclinic nature of polar lows. Because of the low tropopause in Arctic air masses, the weak static stability, and the large Coriolis parameter, maximum baroclinic wave growth is expected to occur for much smaller horizontal scales than at midlatitudes (see, e.g., Holton 2004, 230–238), which is consistent with the observed size of polar lows (200–500 km in diameter). Recently, Bracegirdle and Gray (2008), in a climatological study, found evidence for polar lows over the southern Norwegian Sea being of “type C” (Plant et al. 2003), meaning that they are driven by an interplay between an upper-level potential vorticity (PV) anomaly and latent heating. Farther north, on the other hand, Bracegirdle and Gray (2008) typically found stronger baroclinic and weaker convective contributions. The model-based polar low studies of Mailhot et al. (1996) and Førre et al. (2011a, manuscript submitted to

Quart. J. Roy. Meteor. Soc.) obtained extremely high sensible heat fluxes (1,200–1,400 W m^{-2}) near the ice edge, and the latter study found sensible heating to be a crucial factor in explaining the polar low deepening. The field campaign described below seeks to provide observational data that will enable scientists to validate these diverse conceptual models, while at the same time providing a test bed for the NWP models, thereby contributing to improved forecasting of polar lows.

Shallow Arctic fronts define the southern extension of the cold Arctic boundary layer originating over sea-ice/land and may extend several hundreds of kilometers southward during major cold air outbreaks. The stable air of the frontal zone is eroded by a convective boundary layer building up over the sea, and model simulations indicate that the corresponding large surface fluxes and release of latent heat are important for the frontal circulation (Grønås and Skeie 1999). Although their small spatial scale precludes routine detection, shallow Arctic fronts generating strong winds are believed to occur frequently in situations with off-shelf flow in winter. Only two detailed observations of Arctic fronts exist (Shapiro et al. 1989; Drue and Heinemann 2001), and new observational data are essential for a better understanding of the phenomenon.

When the stable Arctic air impinges on the mountains of Spitsbergen, strong jets and downslope winds can occur, aided by drainage and katabatic flow from the ice sheets over the interior of Svalbard, and the flow becomes highly nonlinear. For instance, Skeie and Grønås (2000) found speed-up factors larger than 2 relative to the upstream wind speed in easterly flow impinging on Spitsbergen. Previous studies also indicate that in order to simulate such wind storms, very high spatial resolution is required (e.g., Sandvik and Furevik 2002). These previous studies are almost exclusively model based, and there is an urgent need for observational data to validate the model simulations.

The purpose of this paper is to describe a field campaign, operated out of Andøya in northern Norway in 2008, gathering unique atmospheric data on the weather phenomena described above. The campaign was jointly funded by the Norwegian Research Council, the German Aerospace Center [Deutsches Zentrum für Luft- und Raumfahrt (DLR)], and the European Facility for Airborne Research (EUFAR). One of the international clusters within the International Polar Year effort was IPY–THORPEX, consisting of, e.g., the Greenland Flow Distortion experiment (GFDex; Renfrew et al. 2008), Storm Studies in the Arctic (STAR; Hanesiak et al.

2010) and the Norwegian IPY-THORPEX, which we here report on. IPY-THORPEX is linked to the THORPEX program of the World Meteorological Organization (WMO), and the overall objective of the Norwegian IPY-THORPEX project is to improve the accuracy of high-impact weather forecasts in the Arctic region. In order to achieve this objective, the following research activities were initiated: (i) a comprehensive field campaign in the late winter of 2008 described herein, (ii) investigations of the synoptic-scale conditions preceding the development of the phenomena responsible for Arctic weather extremes, (iii) the development of a probabilistic forecasting system [the Limited-Area Model Ensemble Prediction System (LAMEPS)] for the Norwegian Arctic, and (iv) enhanced use of new satellite data, in particular from the IASI instrument on the European polar satellite MetOp.

The field campaign sought to address the following research questions:

- What is the relative role of low-level baroclinicity, upper-level forcing, surface fluxes and latent heat release from deep convection for polar low development?
- To what extent can conceptual models from hurricane theory (CISK, WISHE) be applied to polar lows?
- Is there a potential for improving weather forecasts (deterministic as well as ensemble) in the Arctic through targeted observations by aircraft?

It also was designed to meet the following needs:

- Documenting the structure of Arctic fronts
- Investigating the capability of airborne lidar systems to capture mesoscale wind and humidity structures in the Arctic
- Leaving a legacy for future research by providing unique high-quality observational data to the international scientific community
- Leaving a legacy for weather forecasting by providing and exploiting new observational platforms [e.g., unmanned aerial systems (UAS)] in the data-sparse Arctic region

In the following section, a general overview of the 3-week campaign is presented. In the section “Campaign snapshots” we present results from data gathered during selected flights, followed by a section on the use of targeted observations during the campaign. In the section “Leaving a legacy” the future directions for observations in the Arctic are

discussed, before presenting a summary and the main conclusions of the study in “Concluding remarks.”

OVERVIEW OF THE CAMPAIGN AND SYNOPTIC CONDITIONS.

The 3-week campaign took place during the period 25 February–17 March 2008, with a base of operations at Andøya on the Atlantic coast of northern Norway, at 69°N, 16°E, some 280 km north of the Arctic circle (Fig. 1). The main measurement platform of the field campaign was the German research aircraft DLR Falcon, equipped with three measurement systems: (i) probes for in situ measurements of the turbulent fluctuations of the three-dimensional wind, temperature, and humidity; (ii) two lidar systems retrieving profiles of humidity and wind; and (iii) dropsondes that continuously measure wind, temperature, humidity, and pressure as they fall through the atmosphere. The technical features of the instruments are described in appendix A. A total of 12 missions were flown, in three cases with refueling at Spitsbergen, and the total number of flight hours was 55. A total of 150 dropsondes were released during the 12 missions, and all of the retrieved observations were transmitted onto the Global Telecommunication System (GTS), thereby influencing the operational model analyses at the time. An overview of the flights is presented in Table 1, while Fig. 1 shows the flight tracks and the geographical area. All the observational data of

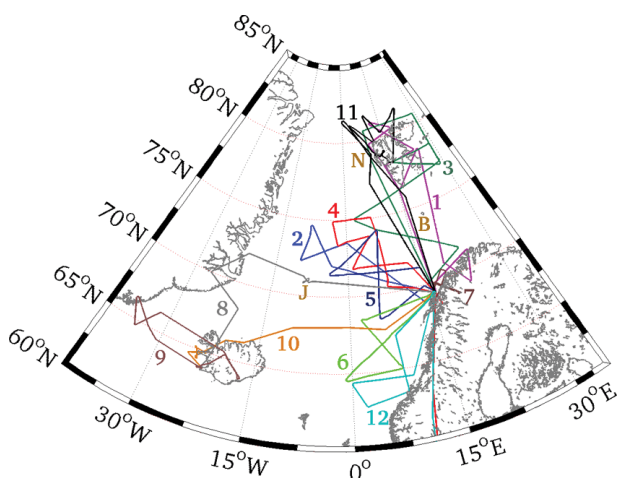


FIG. 1. An overview of the flights during the 3-week field campaign 25 Feb–17 Mar 2008. The numbers refer to flight numbers in Table 1. The campaign headquarters were at Andenes on the coast of Norway, at 69°N, 16°E. Flights 1, 3, and 11 had refueling at Longyearbyen, Svalbard at 78°N, 16°E, while flights 9 and 10 took off from Keflavik, Iceland at 64°N, 23°W. The letters J, B, and N indicate geographical locations referred to in the text: J = Jan Mayen; B = Bear Island; N = Ny-Ålesund.

TABLE 1. An overview of the 12 missions that were flown during the campaign. In all 56 flight hours were carried out, releasing 150 dropsondes.

Mission #	Date	Objective	Flight hours	Dropsondes
1	27 Feb	Svalbard gap flows	6h 50min	8
2	28 Feb	Reversed Arctic front	3h 50min	15
3	1 Mar	Polar low Barents Sea	7h 50min	19
4	3 Mar	Polar low Norwegian Sea	4h 05min	20
5	3 Mar	Polar low Norwegian Sea	3h 45min	15
6	4 Mar	Polar low Norwegian Sea	3h 30min	20
7	6 Mar	Lee flow in northern Norway	3h 45min	8
8	9 Mar	Barrier flow in eastern Greenland	3h 55min	6
9	10 Mar	Orographic winds Iceland	4h 10min	6
10	11 Mar	Targeting northeast of Iceland	3h 45min	6
11	15 Mar	Cold air outbreak Svalbard	7h 15min	14
12	17 Mar	Polar low Norwegian Sea	3h 25min	13

the campaign are made available to the international community via the IPY Data and Information Service (<http://ipydis.org/>), as described in appendix B.

Surface fluxes of sensible and latent heat, which are important ingredients in polar lows, can be measured in situ by flying into the lowest 50 m of the atmosphere and exploiting the turbulent probes on the aircraft. This was done by the DLR Falcon in the LOFZY 2005 campaign. However, because of the risk of misalignment of the sophisticated lidar instruments on board, it was decided not to fly into the turbulent surface layer. Another possible way of obtaining the surface latent heat flux is by combining the two lidar systems, as described by Kiemle et al. (2007). However, this would have required flying in the lower troposphere, which in most of the polar low cases was very cloudy, while at the same time losing the ability to obtain dropsonde profiles through the whole troposphere. Therefore, with one minor exception north of Svalbard on 15 March, all the flights in this campaign were carried out at altitudes of about 8 km. That altitude is ideal both for lidar and dropsonde profiling of the whole troposphere. For the two polar low cases described below, surface fluxes of sensible and latent heat were estimated from bulk formulas using near-surface temperature and humidity from the dropsondes, combined with sea surface temperatures (SSTs) from model analyses (Før et al. 2011b). The results of these calculations will be discussed below (note that Fig. 10 is based on such a calculation).

To complement the aircraft observations, the campaign was augmented by surface observations: Two Norwegian coast guard vessels released radiosondes

on demand within the area of interest. Additional 6-hourly radiosonde releases were carried out at the Norwegian Arctic stations Jan Mayen, Bear Island, and Ny-Ålesund. In collaboration with the integrated Arctic Ocean Observing System (IAOOS), drifting buoys supplied observations of sea-level pressure and near-surface winds. Finally, two unmanned aerial systems were deployed at Spitsbergen for measurements of the Arctic atmospheric boundary layer. The larger one, a CryoWing with a wingspan of 3.8 m and a maximum takeoff weight of 30 kg (http://uas.norut.no/UAV_Remote_Sensing/CryoWing.html), operated by the Northern Research Institute (NORUT) in Tromsø, was stationed close to Longyearbyen. The smaller one, a Small Unmanned Meteorological Observer (SUMO; Reuder et al. 2009)—a lightweight micro-UAS with a wingspan of 80 cm and a takeoff weight of 580 g, developed and operated by the Geophysical Institute, University of Bergen (UiB)—was used as a “recoverable radiosonde” both on land and during a cruise around Spitsbergen from the helicopter deck of the Norwegian Coast Guard vessel *KV Svalbard*.

Following the mildest December–February (DJF) period on record in northern Norway, the weather pattern changed dramatically during the last week of February, such that two out of the three weeks of the campaign were dominated by cold Arctic air masses over the area of interest (shown in Fig. 1). This is shown in Fig. 2, expressed by the dimensionless MCAO index, which is approximately equivalent to the difference between the SST and the potential temperature at 700 hPa in kelvins (Bracegirdle and Kolstad 2010) and is therefore a good measure of the vertical stability in the lower troposphere. Typical MCAO index values

during polar lows range from 2 to 20, with an average in the 5–10 range. The figure displays the daily mean MCAO index from 1 February to 30 March 2008 defined along the 71°N latitude line in the Atlantic sector. During the first 10 days of the campaign (25 February–6 March) the MCAO index values were about 5–10 units higher than the climatological mean in this region (about –5 to 0 during winter), as a cold upper-level low dominated the flow pattern (not shown). This was the period when several polar low developments took place, including the 3–4 March polar low, which is extensively described below. Seven flight missions with a total of 35 flight hours were flown in this 11-day period. On 7 March, the atmospheric flow patterns started to change, with warmer air masses advancing into the Norwegian and Barents Seas over the following days. Consequently, the attention was shifted to the Greenland–Iceland area, where northerly flow prevailed, and the next three missions were carried out in that region (Table 1), studying barrier flow generated by Greenland's orography, as well as wind patterns generated by isolated mountains in Iceland (see, e.g., Ólafsson and Ágústsson 2007). Then, starting on 15 March, a sustained period with high MCAO index values, at times more than 10 units higher than the climatological mean, occurred in most of the region east of the 0° meridian.

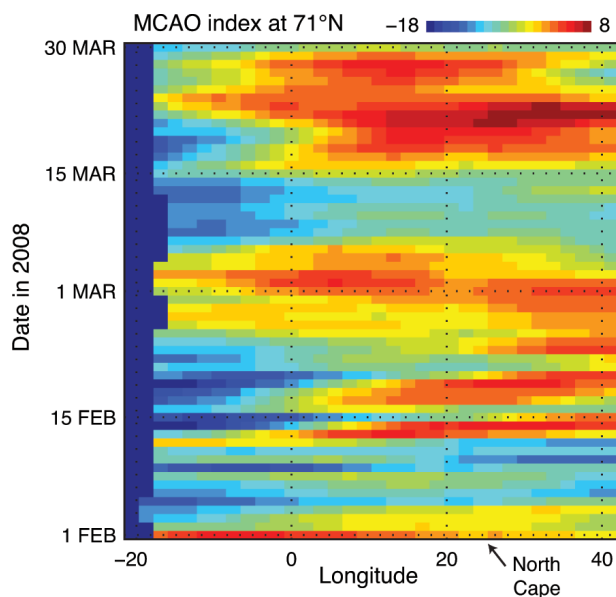


FIG. 2. The MCAO index for each NCEP reanalysis grid point along latitude 71°N in the Atlantic sector from 1 Feb to 30 Mar 2008. The dark blue cells on the far left are due to the presence of sea ice. The dashed black lines delineate the campaign period 25 Feb–17 Mar 2008. The climatological average of the MCAO index during the winter in this region is about –5 to 0.

Months before the campaign, a flight plan strategy document for the campaign was written (Barstad et al. 2008). Different weather scenarios were worked out and flight plans were made. During the campaign a group of about 30 scientists and technicians from several institutions and as many as 11 countries had their headquarters at the Andøya Rocket Range (<http://rocketrange.no>), only 4 km from the airport at Andøya where the DLR Falcon was based. A core group of about five scientists carried out the day-to-day flight planning and were in close dialog with the DLR crew and technicians. For the flight planning, in addition to rapid Internet access, the scientists also had direct access to up-to-date analysis and forecast products of the Norwegian Meteorological Institute (NMI), making extensive use of the graphical software DIANA. In addition, they were in occasional contact with on-duty forecasters at the NMI regional office in nearby Tromsø, who have for the last 5–10 years had a special focus on polar low forecasting.

CAMPAIGN SNAPSHOTS. We now describe some results from selected flights during the campaign, giving a flavor of the different weather phenomena that were encountered, as well as some of the associated weather forecasting issues.

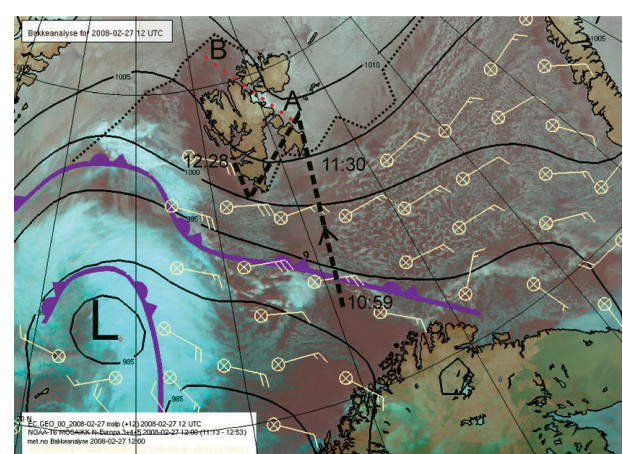


FIG. 3. The weather situation at 1200 UTC 27 Feb 2008, depicted by an infrared satellite image (NOAA-16 channel 4) overlaid with fronts and symbols from the Norwegian Meteorological Institute's subjective analysis, sea-level pressure from ECMWF analysis (black contours), and QuikSCAT-derived 10-m winds (wind barbs). The QuikSCAT wind data are from the time window 0900–1500 UTC. The thick dashed black lines outline the section shown in Fig. 4, while the red dotted line A–B indicates the position of the cross section in Fig. 5. The ice edge is shown by a dotted black line.

Orographic winds at Spitsbergen. On the first full day of the campaign, 26 February, a decision was made to fly a double mission on the following day, with the objective of measuring 1) air mass contrasts across a stationary front over the Barents Sea and 2) terrain-induced disturbances in the vicinity of the main Svalbard islands, Spitsbergen and Nordaustlandet (separated by a dotted line in Fig. 3). Figure 3 displays the weather situation for 1200 UTC 27 February 2008, showing a stationary front oriented northwest–southeast over Bear Island ($74^{\circ}18'N$, $19^{\circ}06'E$), dividing the air masses in the Barents Sea. Relatively warm air resides to the southwest, while the northeast sector is dominated by Arctic air moving westward, leading to cloud street formation over the relatively warm ocean. When the cold and stable air in the northeasterly flow impinges on the Spitsbergen orography, some lifting is expected as the air—at some vertical level—flows over the mountains. Linear theory for flow over topography (Smith 2002) indicates that whenever stable air rises (sinks), a positive (negative) pressure anomaly is expected at the surface. As surface air approaches this positive anomaly upstream of the mountains, it is forced to slow down, and rotational effects yield a diversion of the air to the left of the mountains (in the Northern Hemisphere). This is evident in Fig. 3 where the model analysis shows a tight sea-level pressure field, and elevated Quick Scatterometer (QuikSCAT) winds (15 m s^{-1}) observed near the southern tip of Spitsbergen. Fortunately, we were able to obtain exceptionally good coverage and range with the lidars on this day. The humidity lidar scan (Fig. 4, upper panel) shows the much lower near-surface specific humidity over the sea near Svalbard (at 400–500 km in the figure) than over the open ocean. At 2–6 km it shows structures possibly associated with mesoscale circulations. The gaps in the display are mainly due to clouds, which cause a rapid saturation of the laser beam. From the wind lidar scans (Fig. 4, lower panel), the most spectacular feature is the near-surface wind speed exceeding 20 m s^{-1} near the southern tip of Spitsbergen (just before 1216 UTC in the figure), as well as in outflow areas from the fjords on the west coast of the island (e.g., the Hornsund fjord soon after 1216 UTC and the Van Mijen fjord just before the end of the section). The low-level wind direction from the lidar scans (not shown) is east-northeasterly, parallel to these fjords. These observations are particularly interesting because the observed winds are several meters per second stronger than those predicted by the operational NWP models at the time. The large data gap in the wind lidar near 600 km is due to a lack of aerosol backscatter in the pristine Arctic troposphere.

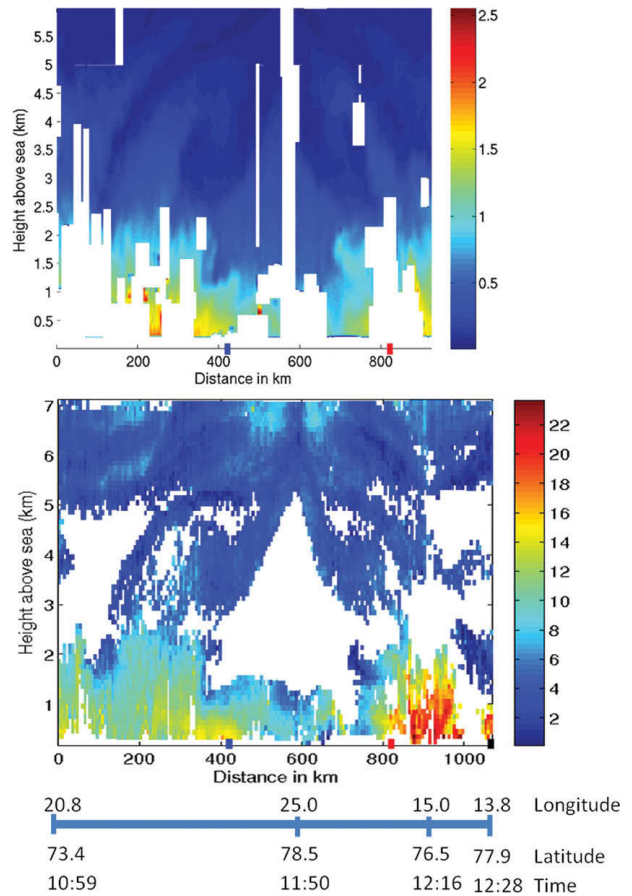


FIG. 4. Lidar measurements along the track of flight I (track shown in Fig. 3) from northern Norway to Spitsbergen between 1100 and 1228 UTC 27 Feb 2008. (top) Specific humidity (g kg^{-1}); (bottom) horizontal wind speed (m s^{-1}). The blue mark just after 400 km indicates the location of the ice edge, while the red mark denotes where the aircraft comes in over land slightly north of the southern tip of Spitsbergen. The black mark near the end of the lower panel indicates the Van Mijen fjord. The blue bar below the two panels has tick marks for turning points of the flight track (cf. Fig. 3).

After refueling in Longyearbyen at Spitsbergen, the DLR Falcon took off at 1330 UTC and then flew through the Hinlopen Strait (from A to B in Fig. 3), which separates the islands of Spitsbergen and Nordaustlandet in the Svalbard Archipelago. Five dropsondes were released. Figure 5 shows a vertical cross section where the lidar scans indicate wind speeds up to 20 m s^{-1} in the strait exit. This is corroborated by dropsonde data showing maximum strength at about 200-m height in the same location. From idealized simulations, Gaberšek and Durran (2004) found that increased gap wind along with a heating of exiting air must be due to a net descent in the gap. This is the situation in the Hinlopen Strait,

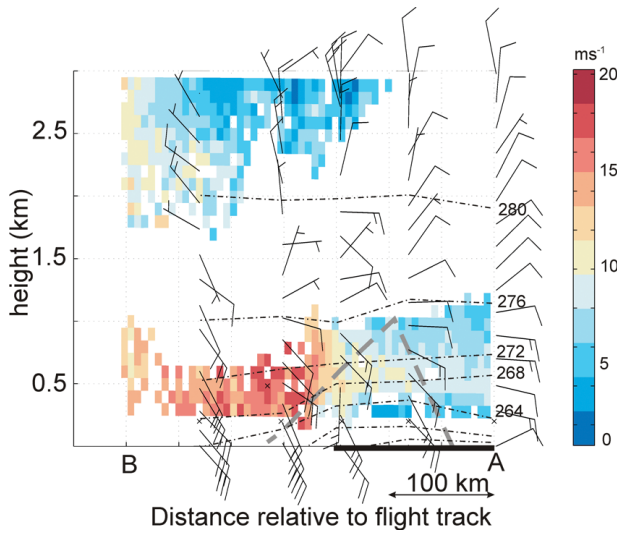


FIG. 5. Cross section through the Hinlopen Strait between 1400 and 1430 UTC 27 Feb 2008, showing retrieved wind speed (color; m s^{-1}) from Doppler lidar scans overlaid with dropsonde wind arrows (one long barb is 5 m s^{-1} ; a short barb is 2.5 m s^{-1}). Horizontal axis indicates the distance (km) in the flight direction. The black, dashed-dotted lines show potential temperature (every 4 K) interpolated from the dropsonde data. The cross section's position is indicated in Fig. 3 as a red broken line. The dashed gray line is the silhouette of the large-scale mountains adjacent to the strait. The thick solid line indicates the sea ice extent.

as observed in the dropsonde dataset: the potential temperature surfaces descend through the strait, as shown in Fig. 5, and at the same time, the wind speed increases. In addition to mechanisms indicated by Gaberšek and Durrant (2004), the open waters on the lee side of the mountains produce positive buoyancy, which may have a significant impact on the flow. A more in-depth investigation of this case is presented by Barstad and Adakudlu (2011).

Reversed arctic front on 28 February.

After missing a poorly predicted polar low north of the island of Jan Mayen ($70^{\circ}59'N$, $8^{\circ}29'W$) on 27 February, the campaign team was keeping a close eye on that area on 28 February, when a new disturbance was expected to develop there, while a weaker system was moving toward Lofoten ($67^{\circ}30'N$, $7^{\circ}33'E$) from the southwest. Interestingly, these two systems, which had different structures and different behavior, were dynamically linked, as seen in Fig. 6a. Figure 6b shows

that the frontal zone is reversed, with the coldest air residing to the south. The reversal is caused by advection of cold air around an upper-level cold low over

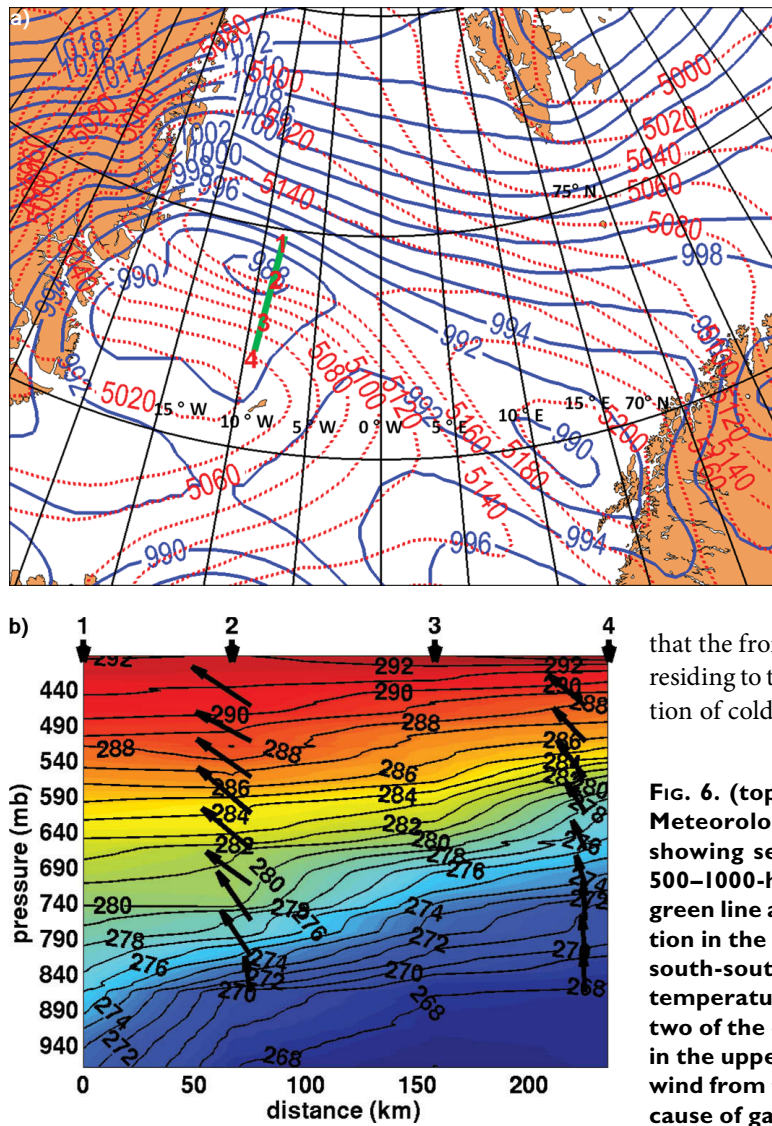


FIG. 6. (top) A surface analysis from the Norwegian Meteorological Institute at 1200 UTC 28 Feb 2008, showing sea level pressure (blue, every 2 hPa) and 500–1000-hPa thickness (red, dashed, every 20 m). The green line and the numbers 1–4 refer to the cross section in the lower panel. **(bottom)** A north-northeast-south-southwest-oriented cross section of potential temperature (K) and horizontal wind (arrows) from two of the dropsondes from the third flight leg shown in the upper panel, between 1244 and 1306 UTC. The wind from the other two dropsondes is not shown because of gaps in the data from these sondes.

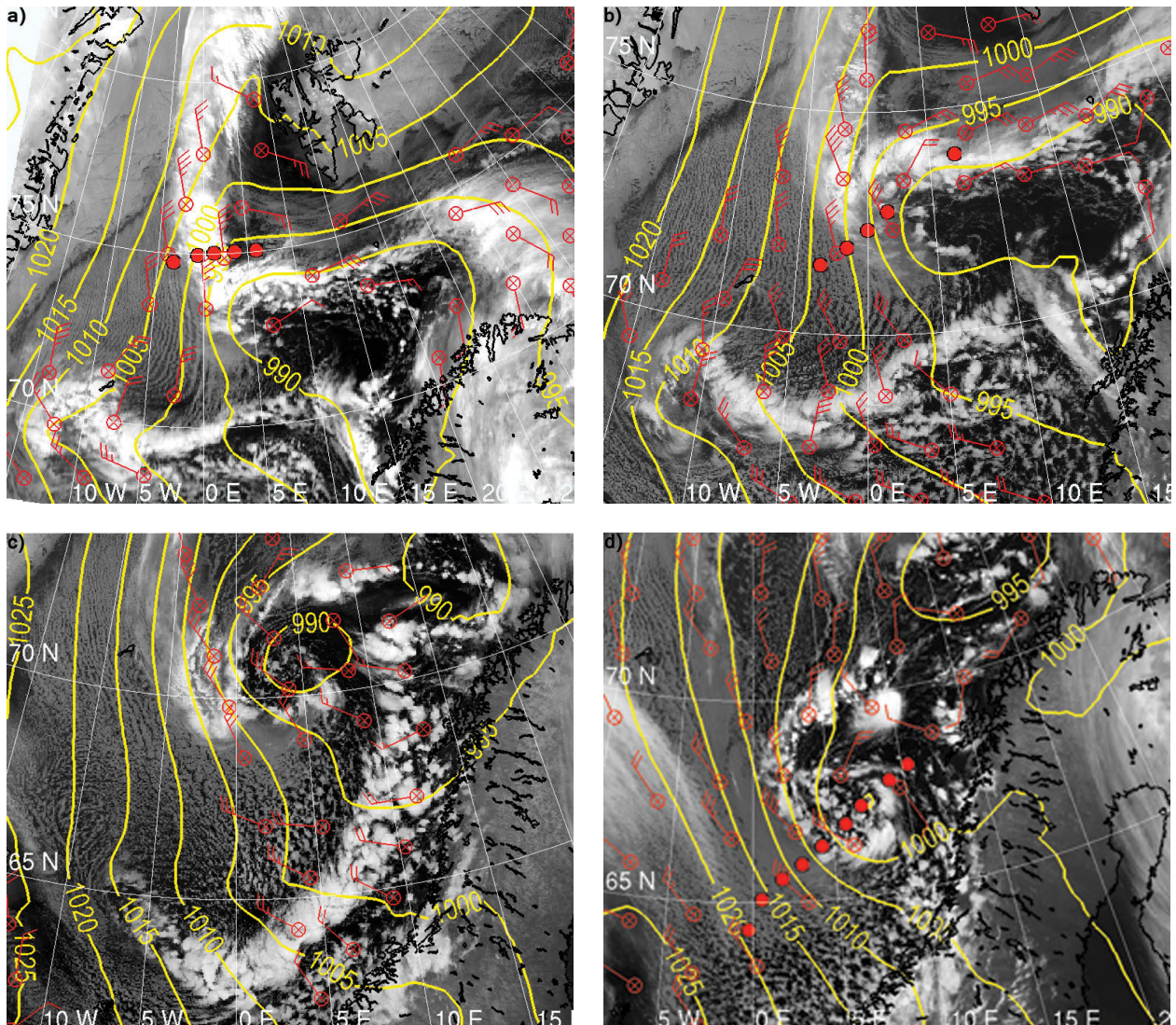


FIG. 7. NOAA AVHRR IR satellite images overlaid with sea-level pressure analyses (every 5 hPa) from the operational Norwegian HIRLAM system and QuikSCAT winds, showing a) a 1200 UTC 3 Mar 2008 analysis combined with the IR image at 1221 UTC; b) a 1500 UTC 3 Mar 2008 analysis, combined with the IR image at 1601 UTC; c) a 0300 UTC 4 Mar 2008 analysis, combined with the IR image at 0307 UTC; and d) a 1200 UTC 4 Mar 2008 analysis, combined with the IR image at 1128 UTC. Red dots indicate dropsonde release positions discussed in the text. Note that the dropsonde points do not coincide exactly in time with the satellite images. The QuikSCAT wind data are from the time window 0900–1500 UTC.

Greenland, while the warm air on the north side has been advected from a southerly direction over the relatively warm waters of the eastern North Atlantic. Associated with the reversed temperature gradient, there was a strong easterly thermal wind, causing a southeasterly upper-level jet of 34 m s^{-1} (Fig. 6b).

Polar low on 3–4 March. In the aftermath of a deep synoptic-scale cyclone, which dissipated off the coast of northern Norway on 2 March 2008, a convergence zone gradually formed along the 0°E meridian, stretching from the sea-ice edge at around 80°N to

about 74°N (Fig. 7a). At the same time, as indicated by the cloud structure in Fig. 7a, another frontal zone, most likely a remnant of a previous frontal system, stretched eastward along 74°N latitude to about 25°E . Based on the available NWP guidance, a polar low was expected to develop near the intersection of these two zones, and it was decided to launch two flight missions on 3 March.

In the northerly flow west of the north–south-oriented frontal zone, evidence of a cold air outbreak is seen as cloud streets developing downwind of the ice edge (Fig. 7a). Farther downwind, near 70°N ,

a cold front is clearly visible at the leading edge of the cold air outbreak, west of 5°E (Fig. 7a), near the island of Jan Mayen (indicated by the letter J in Fig. 1). According to the operational NWP models, this system was not expected to develop further, possibly due to the much lower SSTs in that area.

The surface analysis in Fig. 7a shows the incipient surface low at about 73.5°N and 2°E, with a minimum pressure of about 990 hPa. The first flight took off at 1000 UTC, releasing 20 dropsondes in a “butterfly” pattern (flight 4 in Fig. 1). This pattern was carefully designed to 1) capture the air mass contrasts by flying along the temperature gradients associated with the confluence zones, 2) capture the center of the incipient cyclone, and 3) facilitate the use of the lidar instruments by flying relatively long straight flight legs in the area outside the polar low. A similar strategy was followed on the two subsequent flight patterns into the polar low (flights 5 and 6 in Fig. 1).

Figure 7a indicates the positions of five dropsondes released during one of these legs, crossing the north-south-oriented convergence zone from east to west, and Fig. 8a shows the potential temperature from this section based on the dropsonde data. The most prominent feature is the shallow front, confined below 700 hPa, with the advancing cold air on the western side. Because of geostrophic adjustment in the reversed-shear flow with a southerly thermal wind, there is an associated northerly low-level jet with a wind speed of 26 m s⁻¹ at 940 hPa, detected by sonde number 3 (Fig. 8b).

The second flight took off at 1430 UTC and lasted for 3 h, releasing dropsondes in three straight flight legs. A close inspection of the satellite image about midway into the flight (Fig. 7b) reveals the formation

of an eyelike feature in the polar low, surrounded by cyclonic motion near 73°N, 2°E. The second flight leg stretches from southwest to northeast near the center of the developing polar low (see Fig. 7b). A potential temperature section from this leg (not shown) reveals a warm anomaly between 400 and 800 hPa very close to the cyclone center. Such a downfolding of the potential temperature at upper troposphere level can be an indication of an upper-level PV anomaly (Hoskins et al. 1985). It can also be an indication of descending air.

Overnight, the developing polar low intensified and moved southeast, so that by 0307 UTC a fully developed polar low was clearly discernible in satellite imagery (Fig. 7c). A third flight was launched on 4 March at 1000 UTC, lasting 3 h 15 min, dropping a total of 20 sondes, and seeking to capture the structure of the mature stage of the polar low. Figure 7d shows the polar low at 1128 UTC on 4 March, about midway through this mission. Now, the center of the polar low consists of organized convective cells, with a spiral-like cloud band curving to the northeast being the only remnant of the convergence zone that was so well defined one day earlier. Farther south, the Arctic front that was seen near Jan Mayen in Fig. 7a has now reached the Norwegian coast. The first flight leg, releasing nine dropsondes, was a straight cut through the low in a direction from northeast to southwest (see marks in Fig. 7d). Figure 9a shows the relative humidity from these observations. At the mature stage the polar low is characterized by towers of moist air, with relative humidity values above 80% observed all the way up to 500 hPa. A very interesting feature in Fig. 9a is the dry upper-level air found in sonde 4. This sonde was dropped close to what looks like an

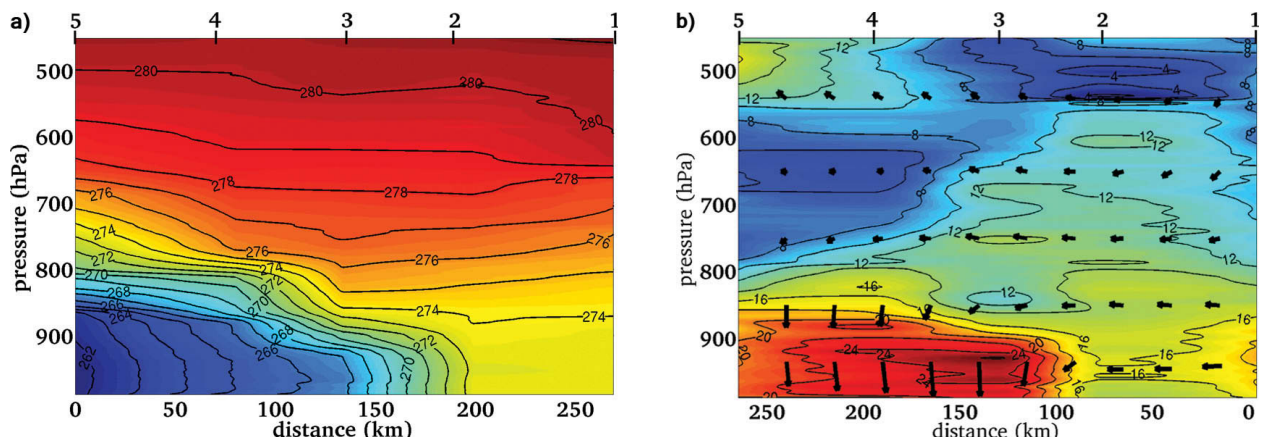


FIG. 8. West–east-oriented cross sections, based on dropsondes from the first flight on 3 Mar 2008 (indicated in Fig. 7a), between 1127 (at 75°04'N, 6°00'E) and 1152 UTC (at 74°46'N, 3°17'W), showing (a) potential temperature (K) and (b) horizontal wind speed (m s⁻¹) and horizontal wind direction (arrows, scaled in size according to the wind speed).

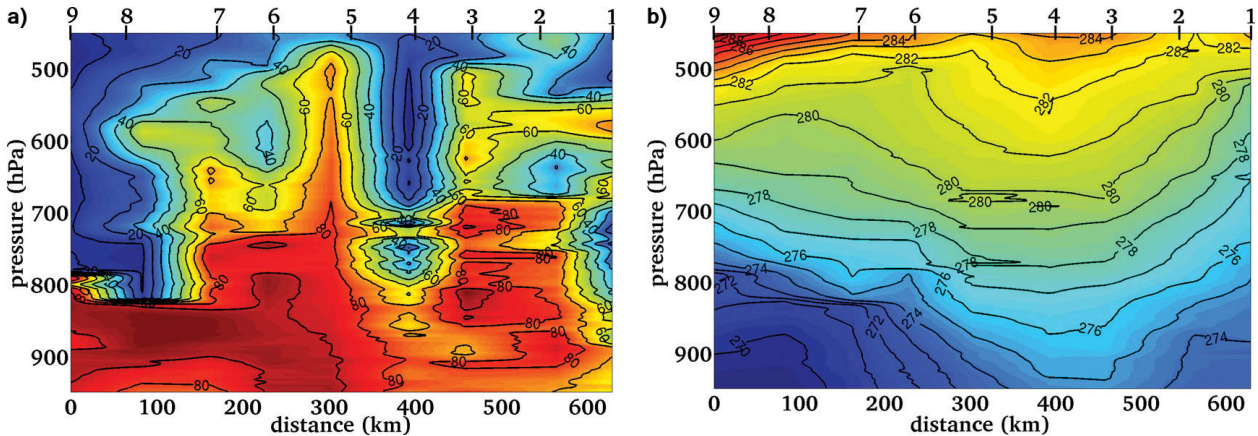


FIG. 9. (left) Southwest- to (right) northeast-oriented cross section based on dropsondes from the flight on 4 Mar 2008 (indicated in Fig. 7d), between 1041 (at $68^{\circ}06'N$, $10^{\circ}19'E$) and 1132 UTC (at $64^{\circ}32'N$, $0^{\circ}27'W$), showing (a) relative humidity (%) and (b) potential temperature (K).

eye in the satellite image in Fig. 7d. Figure 9b shows the potential temperature in the section through the cyclone. On the cold side (left) the tropopause is located at about 500 hPa, which is also the height of the convective towers seen in Fig. 9a. The central core of the cyclone (dropsonde 4) is characterized by warm air and weak static stability, which, combined with the dry feature seen in Fig. 9a, may indicate intrusion of stratospheric air near the center of the cyclone. A corresponding cross section of specific humidity (not shown) confirms this dryness, with values of, for example, below 0.4 g kg^{-1} at 750 hPa, as compared to about 1.0 g kg^{-1} in the surrounding dropsondes. At 1800 UTC, a few hours after the flight on 4 March, the polar low made landfall at $64^{\circ}N$, $10^{\circ}E$. As it did so, 20 m s^{-1} winds and snowfall were observed at Hitra island, about 100 km farther west-southwest.

As mentioned earlier, Føre et al. (2011b) used the dropsonde data from 3–4 March to calculate surface fluxes of sensible and latent heat. Already, during the incipient stage on 3 March (Fig. 7a), they found sensible heat fluxes of about 250 W m^{-2} and latent heat fluxes of about 200 W m^{-2} in the cold air outbreak to the west (rear) of the polar low. On the following day when the polar low had reached maturity, the sensible and latent heat fluxes had increased to about 300 and 350 W m^{-2} , respectively. These latter values can be compared to the direct measurements by Brümmer et al. (2009) and the observational estimates by Shapiro et al. (1987). The former study had maximum sensible heat fluxes similar to those of Føre et al. (2011b), but the maximum latent heat flux in Brümmer et al. (2009) of 520 W m^{-2} was much higher than obtained for the 4 March 2008 case. These differences may be related to the somewhat stronger winds in Brümmer's case yielding generally

higher fluxes, combined with the fact that the sea surface temperatures in the Norwegian Sea south of $70^{\circ}N$ are much higher than in the Barents Sea, which would tend to boost the sensible heat flux. The flux estimates of Shapiro et al. (1987) of 500 W m^{-2} for sensible as well as for latent heat flux are considerably higher than those of Føre et al. (2011b), and that can be attributed to the stronger winds in Shapiro's case: 35 m s^{-1} , as compared to about 25 m s^{-1} on 4 March 2008. Clearly, the different methods used to obtain the estimates in these three cases may also influence the results.

A major asset of having so many flights in conditions with polar lows is the ability to test and validate numerical and conceptual models of polar lows. The campaign data have already been used by Linders and Saetra (2010) to address the questions of possible mechanisms for polar low deepening described in the introduction. Using all dropsondes from polar-low-like conditions during the campaign, they calculated CAPE and convective inhibition (CIN). Invariably they found CAPE values to be very small, in most cases on the order of 100 J kg^{-1} or less. This led the authors to reject CISK as a likely mechanism for polar low development. They attributed the low CAPE values to the small time scale by which the convection exhausts the excessive potential energy that is continuously produced by the heating of the atmosphere from below in the cold air outbreak. They further attributed the discrepancy of their CAPE values with the previous estimate of a CAPE reservoir by Rasmussen et al. (2003) to the use of inaccurate National Centers for Environmental Prediction (NCEP) analyses in that study. In this way, the campaign data are already changing our understanding of polar low dynamics.

As opposed to the polar low on 27 February (mentioned above) and the polar low to be described below (on 16–17 March), the 3–4 March polar low was remarkably well predicted 24–36 h in advance (not shown), making flight planning easier than expected. Flight plans for the incipient stage of the polar low early on 3 March that were designed on 2 March only needed minor adjustments before takeoff. Likewise, the second flight on 3 March and the flight on 4 March successfully followed plans made up to half a day earlier. It is likely that the high predictability of the polar low in the early stages (Figs. 7a,b) was related to the frontal zones stretching to the north and east being well resolved in the models. Polar lows that do not have such well-defined baroclinic features are likely to be less predictable. Flight planning for the following day, 4 March, may on the other hand have been aided by the influence of the dropsondes on 3 March, which may have improved the predictability for that day (cf. the section on p. 14 titled “The impact of targeted observations on a deterministic forecast”).

Polar low on 16–17 March 2008. In connection with the MCAO over the Norwegian and Barents Seas starting on 12 March (see Fig. 2), conditions for polar low development gradually became more

favorable over the following days. The “favorable conditions” were indicated by various factors previously shown to accompany polar low developments (e.g., Blechschmidt et al. 2009): a temperature difference between the sea surface and 500 hPa exceeding 40 K (Noer and Ovhed 2003), the existence of an upper-level (500 hPa) low in the area of interest, and a PV anomaly propagating along the tropopause approaching the area of interest.

It was decided to fly over the area west and north of Spitsbergen on 15 March, dropping sondes at selected points along the transit from Andøya (Fig. 10), in order to capture the initial cold air outflow, which was expected to initiate a polar low development several hundred kilometers farther south. As Fig. 10 shows, the flight track crossed a pronounced baroclinic zone, with the 500–1000-hPa thickness decreasing from 5,220 m at the first dropsonde (at 71°N, 15°E) to 4,960 m at the last dropsonde (at 81°N, 2.5°E). Just west of the flight track there was a rather sharp southeast–northwest-oriented warm core trough, which had slightly deepened over the preceding 12 h (not shown). Associated with the trough were distinct cloud features (not shown), while the air was less cloudy in the high pressure ridge to the south and southeast of Spitsbergen. The cross sections based on the six soundings (Figs. 11a,b) reveal the contrast between the dry, stable Arctic air to the north (surface temperature of -28°C over the sea ice) and the more humid, conditionally unstable maritime air to the south. The cross sections also show signatures of the baroclinic features from Fig. 10 (e.g., an inversion near 800 hPa at dropsondes 2 and 3, probably linked to midlevel warm advection in connection with the trough). Another sloping inversion is found going from about 650 hPa at dropsonde 2 to about 550 hPa at dropsonde 3 (Fig. 11a), with a sharp transition to drier air above (Fig. 11b). At the southernmost dropsonde (sonde 1), close to where the polar low developed 12–24 h later, the upper troposphere is moist and less stable than in dropsondes 2 and 3, indicating deep convection.

In Fig. 10 we show the surface fluxes that we computed from the dropsonde data, as described above. We note that with the exception of

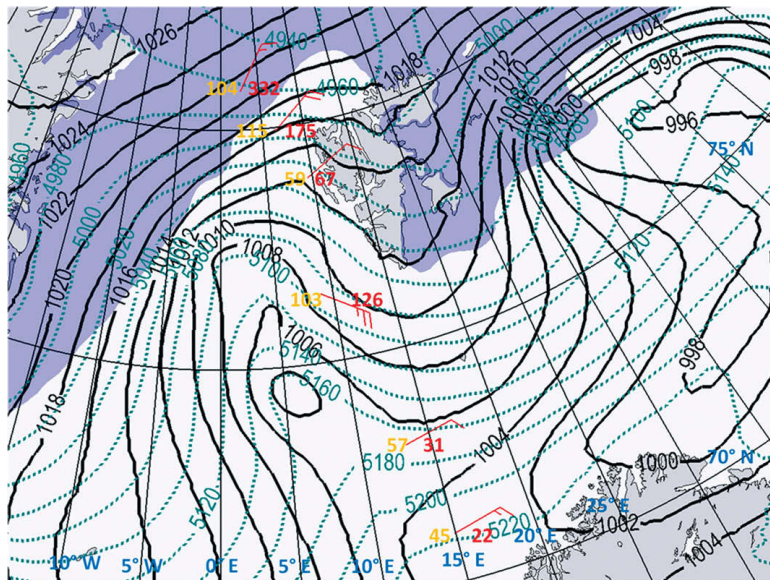


FIG. 10. Analyses by the Norwegian HIRLAM12 model of sea level pressure (black solid lines, every 2 hPa) and 500–1000-hPa thickness (green, dotted lines, every 20 m) at 1200 UTC 15 Mar 2008. Areas in blue shading are covered with sea ice. Orange and red numbers indicate estimated surface fluxes of latent heat (W m^{-2}) and sensible heat (W m^{-2}), respectively, from dropsondes during the flight on 15 Mar 2008, between 0914 (southernmost dropsonde) and 1055 UTC (northernmost dropsonde), while the wind bars indicate the observed wind from dropsondes at 10 m above sea level. See text for details.

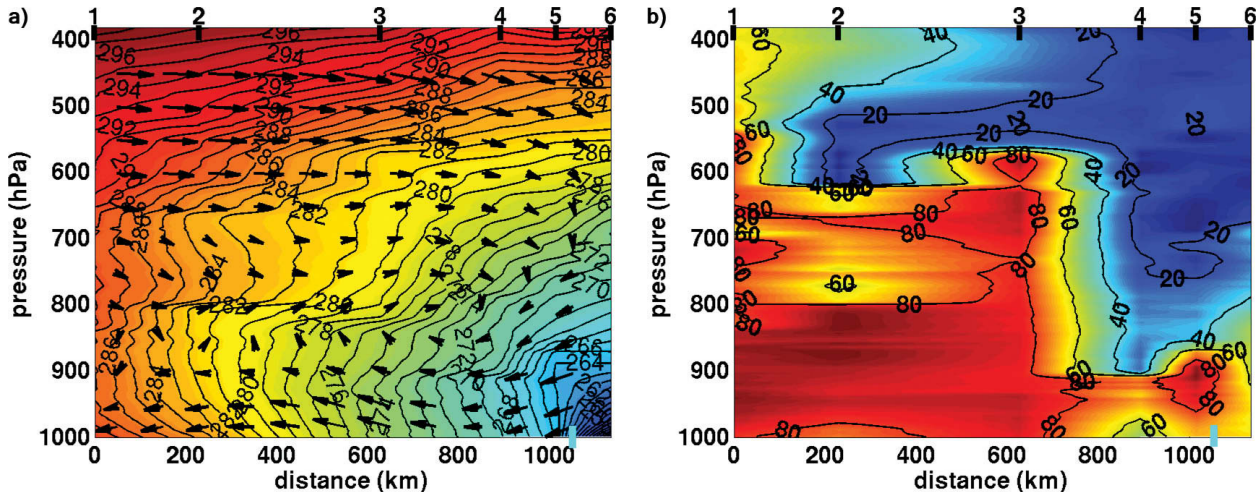


FIG. 11. (left) South-southeast- to (right) north-northwest-oriented cross sections based on the dropsondes from the flight on 15 Mar 2008 (cf. Fig. 10), between 0914 (at 71.0°N , 14.9°E) and 1055 UTC (at 80.8°N , 2.6°E), showing (a) equivalent potential temperature (K) and (b) relative humidity (%). The light blue marks indicate the position of the ice edge, with open water on the left. The arrows in the left panel indicate the direction of the horizontal wind, based on the dropsonde data.

the sensible heat flux at the northernmost dropsonde, all the flux values are below 200 W m^{-2} , and the combined flux is below 300 W m^{-2} . These modest values, compared to those obtained by Føre et al. (2011b) for the 3–4 March case, are mainly due to the rather low wind speeds at this point. Also, we note from the angle between the wind barbs and the thickness lines that the temperature advection near the surface is rather weak at the dropsonde locations.

Unfortunately, because of heavy snowfall at Andøya on the following day (16 March), a planned mission into the mature polar low (Fig. 12) had to be canceled. Therefore we are unable to perform a dropsonde-based comparison of the two polar low cases (3–4 March and 16–17 March), either in terms of structure or surface fluxes.

Compared to the polar low development on 3–4 March, the NWP model guidance turned out to be very poor for the 16–17 March polar low, rendering advance flight planning extremely difficult. Thirty-six-hour forecasts from three operational models at the time—the regional High-Resolution Limited-Area Model (HIRLAM) and the fifth-generation Pennsylvania State University–National Center for Atmospheric Research (NCAR) Mesoscale Model (MM5)-Storm, as well as the global model of the ECMWF—all placed the polar low several hundred kilometers too far southwest, as seen in Fig. 12. Furthermore, the polar lows made landfall 12–24 h too early in most of the models. One possible contributing factor is the lack of strong baroclinic forcing in the 16–17 March case, compared to the 3–4 March

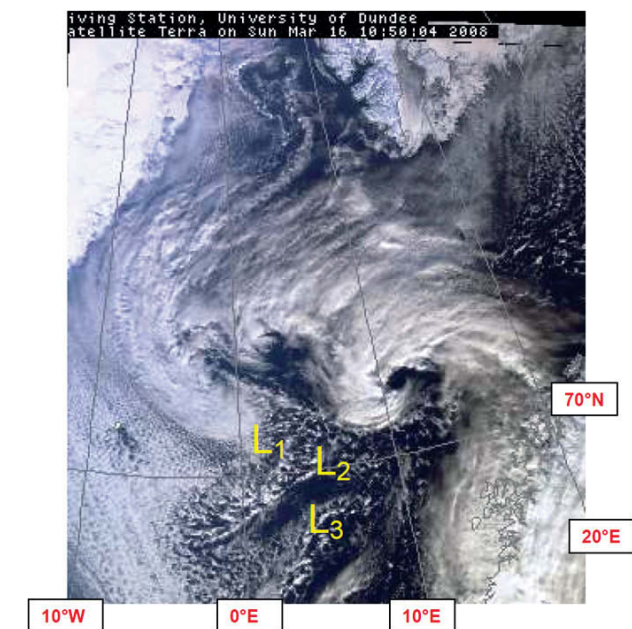


FIG. 12. A MODIS Terra infrared satellite image from 1050 UTC 16 Mar 2008, showing an intense polar low at approximately 71.5°N , 11°E . The image was obtained from the web server of the University of Dundee (www.sat.dundee.ac.uk). Here L_1 , L_2 , and L_3 denote predicted positions (+36 h) of the polar low at 1200 UTC by three major operational models at the time.

case, as evidenced by the frontal-like structures in Fig. 7a. Another factor is the presence of three cyclonic centers, visible at 72.5°N , 2°W ; 72.5°N , 3.5°E ; and 71.5°N , 11°E in Fig. 12. While the westernmost disturbance developed into a polar low in some of the

operational models, it was the easternmost disturbance that developed in reality. It is conceivable that small errors in the initial state or in the model physics may have led the models to develop the “wrong” system. Ongoing investigations seek to answer this question and explore the possible relevance of the so-called dual polar low concept, described by Renfrew et al. (1997) and Brümmer et al. (2009).

THE INFLUENCE OF ADDITIONAL CAMPAIGN OBSERVATIONS ON POLAR LOW FORECASTING.

The impact of targeted observations on a deterministic forecast. Targeted observations are additional meteorological observations that may be used to supplement the routine observing network in data-sparse regions. They are targeted in the sense that they are placed in locations where the forecast for a specified region downstream is sensitive to initial condition errors (so-called sensitive regions). Initial condition errors are more likely to occur in data-sparse areas (i.e., where few routine meteorological observations are available to constrain the first-guess fields). As discussed in the introduction, the European Arctic is data sparse, particularly with respect to high-resolution profile observations.

Previous field campaigns [see Langland (2005) for an overview] have all followed a similar methodology for targeting observations. First, the verification region (i.e., the region that we wish to improve the forecast for) is defined. Next, sensitivity methods are used to determine where the forecast for the verification region is sensitive to initial condition errors, which may result in a large forecast error downstream. Finally, the flight is designed and implemented, trying to cover as much of the target region as possible with additional observations, usually from dropsondes. This methodology may be unsuitable when the key dynamical feature that will affect the forecast in the verification region has itself a scale of only a few hundred kilometers. During the Andøya campaign, the targeting methodology was to exclusively target the polar low that was the main dynamical feature within the area of forecast sensitivity. Predictions of the locations of these regions of forecast sensitivity were provided by the ECMWF Data Targeting Suite (DTS), which was being trialed during the field campaign, for a fixed verification region over Norway. The DTS is part of the Eurorisk Prevention, Information, and Early Warning (PREVIEW) program (www.preview-risk.com). Maps showing the sensitive regions for this verification region were provided twice a day for a forecast lead time (from forecast initialization

to targeting) of 36 h and optimization times (from targeting to forecast verification) of 12, 24, and 36 h. Maps of forecast sensitivity were created using two methods: total energy singular vectors (TESV; Buizza and Montani 1999) and the ensemble transform Kalman filter (ETKF; Bishop et al. 2001). It was noted that during periods of MCAOs the region of maximum forecast sensitivity identified by the ETKF was always over the north Norwegian and Barents Seas, in the region where polar lows form and where the observational network is sparse, whereas the TESV tended to identify areas farther south and west.

We now turn to the polar low on 3–4 March, studied above, and we focus on dropsonde data from the two flights on 3 March. A large region surrounding the polar low was identified as a sensitive region by the ETKF sensitive area predictions, but not the TESV sensitive area predictions. The data from the dropsondes were sent to the global telecommunications system in real time; however, only the sondes from the later flight on 3 March were operationally assimilated into the model analyses (at 1800 UTC), as the sondes from the first flight missed the data cutoff time for the 1200 UTC analysis. To study the impact of these targeted sondes on the forecast for Norway, hindcast studies have been performed using the Met Office Unified Model (MetUM) version 6.1 with a three-dimensional variational data assimilation scheme. The forecasts from 1200 and 1800 UTC 3 March have been rerun on a 24-km grid limited-area domain assimilating either only routine observations, or both routine and targeted observations at 1200 and 1800 UTC. An initial comparison of these forecasts with ECMWF operational analyses shows that the sondes from the 1200 UTC flight did not improve the forecast of the polar low landfall (not shown). On the other hand, the sondes from the 1800 UTC flight did improve the position and intensity of the polar low as it made landfall in Norway (Fig. 13). The ECMWF analysis shows the polar low making landfall at 1800 UTC on 4 March, with the 10-m winds exceeding 21 m s^{-1} to the southwest of the polar low center (Fig. 13c). In the forecast containing only routine observations (Fig. 13b), valid at the same time as the analysis, the polar low has already made landfall farther south, and therefore the region of strong winds is too far south and the winds are weaker. The forecast containing targeted observations from 1800 UTC (Fig. 13a) improves the polar low position and strength, although the region of strong winds extends too far south compared to the analysis. In a separate study by Irvine et al. (2011), the ECMWF analyses for this case were validated using dropsonde and QuikSCAT observations, and a good agreement

was found. Further work is underway to confirm the impact of the targeted sondes on the forecast and the reasons for this impact.

The impact of additional observations on an ensemble forecast. At the Norwegian Meteorological Institute, a 21-member limited-area short-range ensemble prediction system (LAMEPS) has been quasi-operational since February 2005 (Frogner and Iversen 2001, 2002; Frogner et al. 2006). The system was upgraded in November 2007 and in mid-February 2008, providing an extension of the integration domain to include larger parts of the Arctic Ocean and with a grid spacing reduced from 22 to 12 km. Also, two different cloud parameterization schemes were introduced, alternating between the ensemble members, and the forecast frequency was doubled to twice per day. Aspelien et al. (2011) give a comprehensive description and evaluation of the system.

Here we use the spread between the ensemble members to measure random variations relative to the impact of additional campaign observations. The objective is to improve the prediction skill for the polar low over the Norwegian Sea on 3–4 March 2008. The

additional campaign observations are 1) dropsondes from the DLR Falcon aircraft, 2) additional radiosondes from three Russian Arctic stations; 3) additional radiosondes from Norwegian coast guard vessels *KV Svalbard* and *KV Senja*, and 4) additional radiosondes from 0600 and 1800 UTC at Bear Island.

The impact of the additional observations is measured by running two data assimilation cycles in parallel. Thus, a double set of analyses of the atmospheric state is produced every 6 h, and the difference between each pair of analyses is only due to the campaign observations, as interpreted by the data assimilation system. Note that each analysis is a function of the model state, provided as a “first guess,” and the observations. Since observations also influence the first guess through the development of the model state from previous analyses, the impact of the added campaign observations needs to be developed over several data assimilation cycles, unless the extra observations are provided on a specific date only.

The two data assimilation cycles are therefore started (“spun up”) about a week before the actual occurrence of the polar low, from a common operational analysis valid at 0000 UTC 25 February 2008. We use

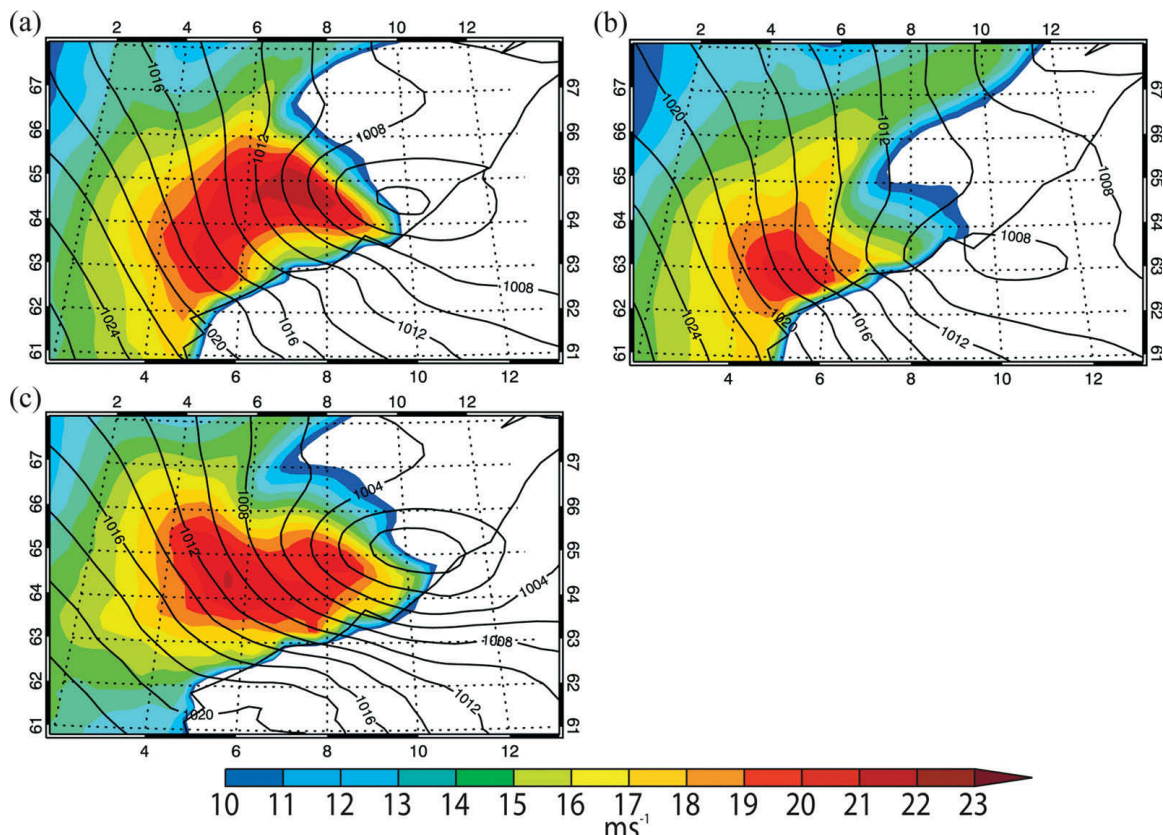


FIG. 13. Sea level pressure (black contours) and 10-m wind speed exceeding 10 m s^{-1} (colored shading) for 1800 UTC 4 Mar 2008, for 24-h forecasts from 1800 UTC 3 Mar 2008 containing (a) routine and targeted observations and (b) only routine observations. (c) ECMWF analysis at 1800 UTC 4 Mar 2008.

the term “clean” to signify the data assimilation cycle that uses regular observations only, and the term “full” for the parallel cycle that additionally employs extra campaign observations. Parallel assimilation

cycles ensure that the full impact of the observations is obtained.

Figure 14 shows selected results illustrating the impact of extra observations on the predictive skill of the polar low. Impacts of the additional observations can be seen in the 47-h forecast valid at 1700 UTC 3 March. The impact of campaign observations on the forecast is measured as the difference between forecasts started from two different analyses both valid at 1800 UTC 1 March, well before the polar low started to develop. By comparing the difference to the forecast ensemble spread, the significance of the impact can be estimated (see below). The polar low developed during the latter half of the nearly 2-day forecast. This situation is challenging for the forecast system but is nevertheless chosen because a 2-day forecast range is crucial for high-impact weather in a region where considerable time for changing operations may be crucial (e.g. fishing boats, ship traffic, off-shore industry, etc.).

The maps in Fig. 14 can be compared to the NOAA satellite image at 1721 UTC, and to 10-m wind observations from the dropsondes that were released during the second DLR flight on 3 March (discussed previously). Figure 14a shows a clear influence of the added campaign observations on the sea-level pressure in the ensemble mean forecast. The polar low can be recognized in the “full” run in connection with a trough (confluence zone) extending westward from a synoptic scale cyclone off the coast of northern Norway. This trough is barely detectable in the clean run, which instead features a weaker trough farther south. Compared to the clean run, the shape of the isobars and the position of the predicted trough in the full run are more in agreement with the 10-m winds from the dropsondes and the position of high clouds from the satellite.

For 10-m wind speed (Fig. 14b) and hourly precipitation (not shown), the two 21-member ensemble sets are different at the 95% confidence level (based on a Wilcoxon–Mann–Whitney nonparametric rank sum test) over considerable areas around the polar low. The large differences in the fields of estimated probability of wind speed exceeding 15 m s^{-1} (more than 60%) and 20 m s^{-1} (more than 10%), seen in Fig. 14b, are related to the large difference in the shape of the isobars (Fig. 14a) near the center of the polar low. The large wind speeds associated with the polar low are better represented by the full run than the clean run. However, the lack of widespread wind observations hampers the evaluation. In this connection it should be mentioned that because of a technical glitch at the Norwegian Meteorological Institute, the satellite-based scatterometer wind observations

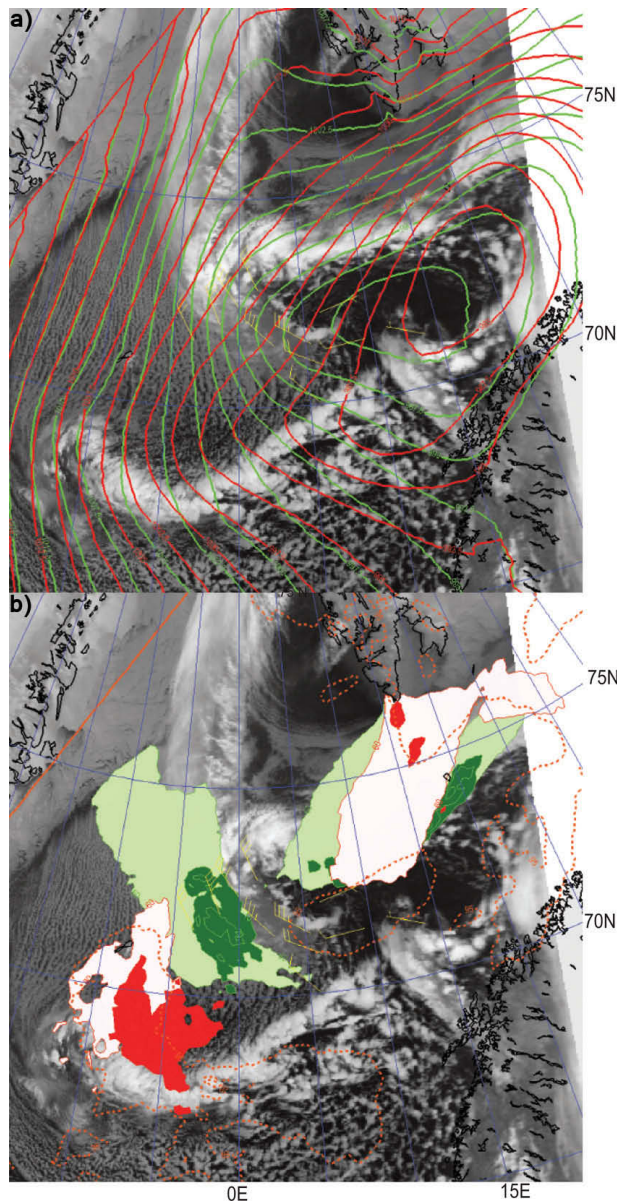


FIG. 14. Results from 47-h LAMEPS forecasts valid at 1700 UTC 3 Mar 2008, overlaid on an infrared (channel 4) NOAA satellite image at 1721 UTC. Observed 10-m winds from dropsondes are shown as yellow wind bars. (a) Ensemble mean sea level pressure from the clean run (red) and full run (green). (b) Light shading indicates more than 60% probability of wind speed exceeding 15 m s^{-1} (light green: full run; light red: clean run); heavy shading indicates more than 10% probability of wind speed exceeding 20 m s^{-1} (green: full run; red: clean run). Dotted lines indicate 95% confidence of difference in 10-m wind speed between the full and the clean run ensembles. See text for details.

available at the time (QuikSCAT) were omitted from the observational basis in the data assimilation cycles. It is quite probable that these observations would have influenced the forecast quality positively.

Thirteen days later (16 March), when another polar low developed in the same area, a similar positive impact was not obtained. The cause of this difference is the subject of ongoing investigations.

LEAVING A LEGACY. IPYs only take place every few decades, and it is therefore important to ensure that the dedicated effort of the IPY is carried on after the end of the IPY itself. This legacy commitment was addressed in the Norwegian IPY–THORPEX by various means, as will now be described. The legacy activities were established as a compromise between what is scientifically desirable and what is feasible given technological, political, and financial constraints.

New observations. One of the goals of IPY was to initiate observations that would continue operation after IPY. The objective of such observations is to fill the observational gap that currently exists in the Arctic, eventually contributing to a new environmental forecasting system for the Arctic (Carlson et al. 2009). In the case of the Norwegian IPY–THORPEX, the following measurement initiatives were taken: 1) the Aircraft Meteorological Data Relay (AMDAR) has been deployed onboard nine Norwegian commercial aircraft flying on routes to northern Norway and Svalbard, significantly enhancing the near-real-time, flight-level, meteorological observations in this region; 2) contributions were made to the development and first field deployment of new UAS for meteorological observations in harsh polar environments; 3) instruments have been deployed for monitoring solar and terrestrial radiation at Bear Island; 4) weather observations in the Russian Arctic were temporarily improved during the spring of 2008; and 5) two automatic weather stations are being deployed on islands southeast of Svalbard during the summers of 2010 and 2011.

Starting in 2009–10, the Norwegian Meteorological Institute launches four upper-air soundings per day instead of two per day during the winter at Bear Island and Jan Mayen, as upper-air soundings are sparse in the Arctic/sub-Arctic and are considered very important for NWP.

On a given day typically 10 flights in northern Norway, including a daily flight to Longyearbyen, report AMDAR measurements between 0600 and 1900 local time. The quantities measured and transmitted are air pressure, temperature, and horizontal wind. The

frequency and location of observations is determined by the Network of European Meteorological Services (EUMETNET)'s AMDAR program. Observations are taken both during landing (every 40 s), takeoff (every 10 s during the first few minutes, relaxing to 40 s), and at flight level en route (every 7 min).

At the time of the IPY–THORPEX campaign two Norwegian groups, NORUT and UiB, had prototypes of unmanned aerial systems ready for first field applications under polar conditions. The main purpose of the deployment of these systems during the campaign was the proof of concept and adaptation of the system to polar conditions, in particular low temperatures, together with the development and test of routines in the interaction with the civil aviation authorities (CAA) for the operation of UAS for scientific purposes. The CryoWing system was stationed at the Old Auroral Station in Adventdalen close to Longyearbyen. Because of limitations concerning flight permissions and technical problems with the launcher unit caused by cold temperatures, the CryoWing system only performed a few test flights at low altitudes in the vicinity of Longyearbyen and without scientific payload. Triggered by the IPY activities and tests, the CryoWing system is now reliably working in the polar environment and to date has performed several successful scientific missions in the field of atmospheric research and surface remote sensing.

The SUMO was previously successfully operated during the “Flow over and around Hofsjökull” (FLOHOF) field campaign in central Iceland in summer 2007, reaching an altitude of more than 3.5 km above ground (Mayer et al. 2011). Because of its low weight and very short preflight preparation times, SUMO was able to get flight permission close to Longyearbyen airport. This enabled around 20 atmospheric profile flights up to a maximum of 1,500 m above ground at the Old Auroral Station in Adventdalen between 4 and 9 March. Before those land-based measurements, SUMO also proved its applicability for ship-based operation. On a cruise with the ice-breaking Norwegian Coast Guard vessel *KV Svalbard* another 10 profiles could be gathered over sea around Spitsbergen in the period 27 February to 1 March, mainly in Storfjorden. Parallel ascents during this cruise have shown that SUMO is able to profile the lower polar atmosphere with an accuracy that is comparable to the usual radio soundings (Reuder et al. 2009). In a follow-up campaign in spring 2009 SUMO performed more than 100 profile flights up to 1,500 m for the investigation of the polar boundary layer around Longyearbyen. The results of

both campaigns—focusing on the value of the UAS measurements on an improved understanding of the boundary layer processes and a related validation of the corresponding parameterization schemes—will be summarized in a separate paper now in preparation.

Nine new automatic weather stations (AWS) transmitting in real time were installed mainly on the eastern part of Svalbard during the summer 2010. They are driven by solar cell power, which in combination with rechargeable batteries with long endurance (5–6 months) ensures continuous operation all year around. The AWS instruments are deployed on a permanent basis and measure air pressure, humidity, temperature, and wind.

Broadband instruments for monitoring solar and terrestrial radiation have been deployed on a permanent basis on Bear Island, supporting the validation of retrieval algorithms for satellite observations. The instrumentation is located at the meteorological station operated by the Norwegian Meteorological Institute, transmitting data in real time to Oslo. Instruments are collocated with surface synoptic measurements of temperature, humidity, clouds, etc., as well as routine radiosonde launches providing atmospheric profiles of temperature and humidity. The solar and terrestrial radiation measurements are used for validation of EUMETSAT Ocean and Sea Ice Satellite Application Facility (www.osi-saf.org/) radiative flux estimates. The deployment of this instrumentation provides a cost-effective and sustainable observational program, making it useful for monitoring, validation, and improvement of parameterizations of radiation in numerical models. In winter the ice edge is usually located close to Bear Island, which makes the station particularly useful for this purpose.

During the IPY–THORPEX campaign Russian upper-air stations in Novaya Zemlya and on the Kola peninsula were equipped to take upper-air soundings more frequently than otherwise, and the data were transmitted in near real time and used by, for instance, ECMWF in their data assimilation. It was also intended to have upper-air soundings at Heiss Island at 80°N, 58°E, but this failed because of a technical problem.

IPY provided the context for establishing a protocol on scientific and technical cooperation between the Norwegian Meteorological Institute and the Russian Hydrological and Meteorological Institute (Roshydromet). The aim of the protocol is to improve the observational basis for weather and ocean forecasts for the polar regions. In this Protocol it is agreed to have 1) cooperation on improving the

observation system in the Barents Sea and adjacent areas; 2) exchange of NWP products in real time; 3) cooperation in utilizing satellite data for forecasting purposes; and 4) exchange of ocean model products (including waves and sea ice) in real time, and cooperative scientific efforts to improve the quality of these products, as well as 5) other areas of activity that may be mutually agreed upon.

Advanced remote sensing methods. During the campaign a novel use of lidar instrumentation for probing of wind and humidity in the Arctic atmosphere was carried out. In particular, the lidars provided invaluable data for the wind events that were studied. In addition to the standard measurements of wind and humidity shown in Figs. 4 and 5, latent heat fluxes can be derived by combining the two lidars, as explained by Kiemle et al. (2007). Considering that surface fluxes of moisture are one of the main energy sources for the polar lows, this is a method that may have a potential for polar low forecasting (e.g., if combined with targeting). Previously DLR wind lidar measurements have been successfully used for targeting purposes (Weissmann et al. 2005).

In order to improve the day-to-day data coverage in the Arctic, we have initiated an implementation of IASI data into the HIRLAM Aladin Regional/Mesoscale Operational NWP in Europe (HARMONIE) data assimilation system. The IASI sensor measures the radiance emitted from Earth in 8,461 channels, ensuring retrievals with a vertical resolution of 1–2 km in the lower troposphere (Collard and Healy 2003). The HARMONIE/Norway limited area model (Randriamampianina and Storto 2008a) was used to explore the impact of the IASI radiances on weather forecasts in the polar region. A set of 366 IASI channels, as proposed by Collard (2007), was extracted from the Meteorological Archival and Retrieval System (MARS) of ECMWF. Active channels showing the best fit to the applied analysis system were selected using a multistep monitoring technique (Randriamampianina and Storto 2008b). The selected 41 channels were most sensitive in high tropospheric and stratospheric layers. The IASI data were assimilated together with most of the conventional and satellite Advanced Television and Infrared Observational Satellite (TIROS) Operational Vertical Sounder (ATOVS) AMSU-A and AMSU-B/Microwave Humidity Sounder (MHS) observations using a three-dimensional variational data assimilation system. Four experiments with cyclic assimilation and subsequent 48-h forecasts were performed during the IPY–THORPEX campaign to evaluate the

impact of the IASI data and campaign observations on the HARMONIE/Norway model analyses and forecasts.

Comparison of the analyses and forecasts against the ECMWF analyses and independent observations showed a positive impact of IASI and campaign observations (Randriamampianina et al. 2011). The IASI data showed positive impact on lower troposphere temperature (Fig. 15), geopotential height in the midtroposphere, and humidity around 700–850 hPa. For the 3–4 March case, a positive impact of IASI data on the analyses and forecasts of polar lows up to 36 h was found, as well as on 24-h forecasts with and without campaign data (not shown).

CONCLUDING REMARKS. An overview has been presented of an aircraft-based field campaign out of northern Norway in the late winter of 2008, with a focus on polar lows, Arctic fronts, and orographic wind storms. In addition to traditional dropsonde releases, the campaign also made use of sophisticated lidar instruments for detailed profiling of humidity and wind in cloud-free air. Such measurements revealed detailed mesoscale wind structures generated by the orography of Svalbard that are not fully resolved by current NWP models. A unique achievement of the campaign was a three-flight probing of the full life cycle of a polar low event over the Norwegian Sea on 3–4 March 2008. The unique dataset thereby obtained has already provided new insight into the existence of reservoirs of CAPE in polar lows (Linders and Saetra 2010). The dropsondes have also been used for estimation of surface fluxes of sensible and latent heat at different times. Also, for that polar low case, targeted observations were shown to improve both deterministic and probabilistic forecasts for the following day. Another spectacular polar low event on 16–17 March 2008 exhibited a much weaker predictability, for reasons subject to continued investigation.

In addition to providing unique datasets to the international community, the project has also left a legacy by 1) developing a new ensemble prediction system for the Arctic; 2) promoting the exploitation of new satellite data (IASI); 3) installing new measurement platforms in the Arctic, both on board commercial aircraft (AMDAR) and on the ground (radiation sensors and automatic weather stations); and 4) contributing to the development and use of unmanned aerial systems for meteorological data sampling in the Arctic.

Ongoing follow-up studies include a detailed study of the 28 February Svalbard wind event by Barstad and

Adakudlu (2011); a comparison of lidar profiles and WRF simulated fields for the 3–4 March polar low by Wagner et al. (2011); a study of the sensitivity of NWP model simulations of the 3–4 March and 16–17 March polar lows to spatial resolution by McInnes et al. (2011); and a thorough investigation of the feasibility of targeting flights by Irvine et al. (2011).

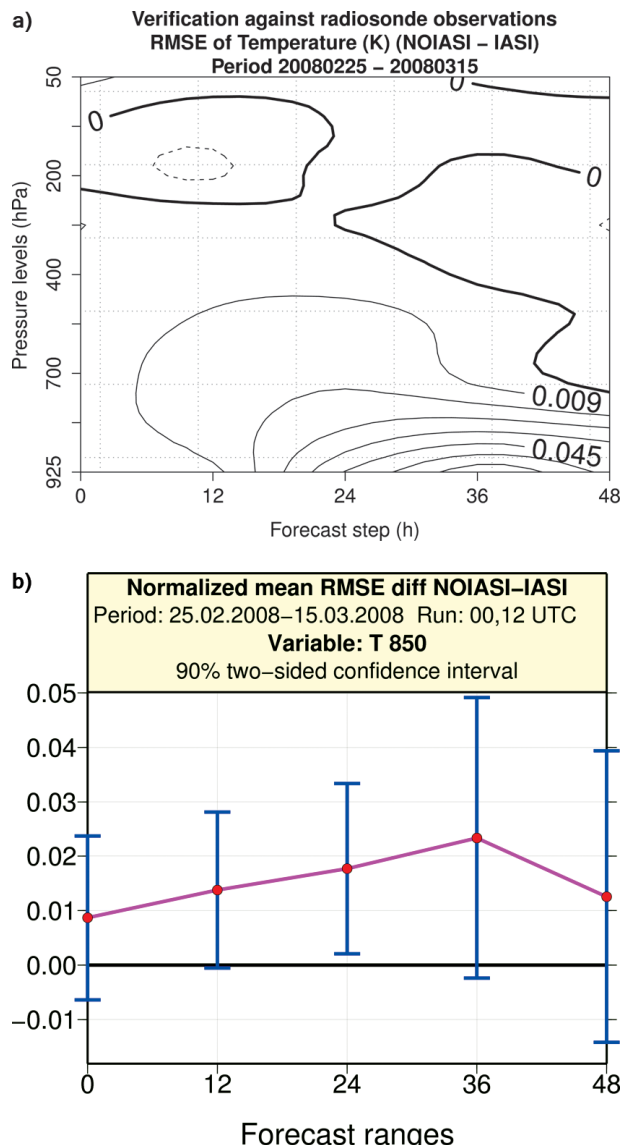


FIG. 15. (a) A time-height section displaying the impact of the IASI data validated against observations (mainly composed of surface and radiosonde data), as measured by the root-mean-square error (RMSE) difference between runs with and without the IASI data, averaged over the whole 3-week campaign period. Positive (negative) values mean positive (negative) impact on forecast quality. (b) The statistical significance of the RMSE difference in (a), based on a *t* test. The error bars represent the interval in which the RMSE difference is significant at the 90% level.

From a climate perspective, one may ask whether the high-latitude weather events studied here will change with global warming, and how that will influence human activities in the region. As the Arctic sea ice retreats, new regions will be commercially exploited, and the human presence is bound to increase. However, with the sea ice gone, these same regions will become exposed to warm, open waters and large heat fluxes from the ocean to the atmosphere. According to projections in the Fourth Assessment Report of the Intergovernmental Panel on Climate Change (IPCC AR4), this is especially true in the eastern and northern Barents Sea and north of the Bering Strait, where steep increases in the MCAO index and thus the potential for polar lows and other convective weather systems are expected (Kolstad and Bracegirdle 2008). The increasing human presence, together with the prospect of worsening weather in these latitudes, provides a strong motivation for enhancing the quality of weather forecasts in the Arctic. This study and its related ongoing research efforts seek to significantly advance Arctic NWP and contribute to the overall IPY achievements.

ACKNOWLEDGMENTS. The Norwegian IPY-THORPEX project was funded by the Norwegian Research Council via Grant 175992/S30. The field campaign also received support from Deutsches Zentrum für Luft- und Raumfahrt (DLR) and from the European Fleet for Airborne Research (EUFAR). In addition, the following institutions and people contributed in various ways to the success of the campaign: the Norwegian Coast Guard, the Andøya Rocket Range, the Andenes Air Force Base, Gunnar Noer, and Gudmund Dalsbø. We thank the DLR pilots, technicians, and scientists for their dedication in connection with the campaign. We thank the two anonymous reviewers for constructive comments, which led to significant improvements of the manuscript. Finally, thanks to Andreas Fix and Stephan Rahm of DLR for helpful comments on the manuscript.

APPENDIX A: AIRCRAFT INSTRUMENTATION. The instrumentation onboard the DLR Falcon during the campaign was as follows:

- a) A 1.8-m-long nose boom for in situ measurements of the three-dimensional wind vector (Meischner et al. 2001). The wind vector relative to the flat ground is determined as the vector difference between the velocity of the aircraft relative to the ground and the velocity of the aircraft relative to the air. The former is given by a global positioning system (GPS) and an inertial reference system (IRS), while the latter is measured using a Rosemount five-hole gust probe (model 858AJ) on the tip of the nose boom. The sensor signals are recorded at 100 Hz, corresponding to a sampling interval of about 2 m. The absolute accuracy of wind measurements is estimated at $0.2\text{--}0.4\text{ m s}^{-1}$ for the vertical wind component and $0.5\text{--}2.0\text{ m s}^{-1}$ for the horizontal wind component.
- b) Sensors on the fuselage measuring temperature, pressure, and humidity at a sampling rate of 100 Hz, using the following instruments:
 - Two deiced temperature probes—more specifically, two Rosemount model 102 deiced platinum (Pt)-resistance total temperature probes). The Pt-wire measures the temperature of air flowing through a special housing, which is formed so as to avoid direct hits of water droplets on the Pt-wire. As the airflow is slowed when passing the sensor element, temperature is increased by a certain amount depending on the airspeed, which is corrected during data evaluation. The accuracy of the measurement is $\pm 0.5\text{ K}$.
 - Three different humidity sensors (http://badc.nerc.ac.uk/view/badc.nerc.ac.uk__ATOM__obs_1162,915,244,899,402), as follows. 1) A Lyman-Alpha Hygrometer Model L-5 made by Buck Research, Boulder, CO. The L-5 measures the absorption of UV radiation at 121.56 nm (the Lyman-alpha line) produced by a hydrogen discharge lamp. The absorption according to Beer's law is a measure of the absolute humidity in the probe path between UV source and detector; 2) A relative humidity sensor, Vaisala Humicap, that is based on the measurement of the capacitance of a small, special ceramic capacitor. The capacity is part of an oscillator. The dielectricity of the ceramic substrate and therefore the frequency of the oscillator are directly related to the relative humidity of the ambient air over a wide range of temperatures. The frequency is transformed to an output voltage, which is recorded. The Humicap provides sufficient calibration stability at medium response times on the order of 1–10 s, depending on the ambient temperature. 3) A Dewpoint Mirror made by General Eastern, model 1011B. The Peltier element cooled DP mirror has the advantage of the best stability and easy absolute calibration. However, because of cooling problems, the response time is rather poor at low absolute humidity levels.

- The Lyman-Alpha and Vaisala sensors are mounted inside the nose of the aircraft with the absorption path respectively the sensing capacitor being inside of a steel tube through which air from outside the aircraft is flowing passively. To correct the changes in the mass density and temperature inside the tube (and therefore the relative and absolute humidity of the air when passing the tube), temperature and pressure inside the tube are measured as close as possible to the probe volumes. The measurement accuracies are $\pm 0.5 \text{ g m}^{-3}$ for absolute humidity measured by the Lyman-alpha instrument, $\pm 2\%$ for relative humidity measurements with the Vaisala sensor, increasing to $\pm 8\%$ at 8 km, and $\pm 0.5 \text{ K}$ at temperatures above freezing and $\pm 1.0 \text{ K}$ at temperatures below freezing for the Dewpoint Mirror.
- Two lidar systems, consisting of a transmitting laser, a telescope, and a detector unit, which invert the backscattered signal to obtain vertical profiles of specific humidity and three-dimensional wind. These are 1) a differential absorption lidar (DIAL) system for humidity measurements (Wirth et al. 2009), which exploits variations in absorptivity near the center of a water vapor absorption line, and 2) a scanning Doppler lidar system for measurements of the three-dimensional wind vector, based on Doppler shift of the received signal relative to the transmitted signal (Weissmann et al. 2005). As explained by Weissmann et al. (2005), the Doppler wind lidar performs a conical step-and-stare scan around the vertical axis with a nadir angle of 20° , resulting in a cycloid scan pattern.

The usefulness of the lidar measurements is limited by their inability to penetrate optically thick clouds. Furthermore, the wind lidar depends on backscattering from aerosols, which may limit its capability in extremely clean Arctic air. The technical properties of the lidar systems are outlined in Table 2.

- Dropsondes (Vaisala RD93). These dropsondes use the NCAR GPS dropsonde system, also known as the Airborne Vertical Profiling System (AVAPS). The dropsondes measure pressure, temperature, humidity, and horizontal wind, transmitting the data back to the aircraft. The accuracy of the soundings is $\pm 1 \text{ hPa}$, $\pm 0.1 \text{ K}$, $\pm 5\%$, and $\pm 0.5 \text{ m s}^{-1}$ for pressure, temperature, relative humidity, and wind speed, respectively. The quality control of the data is done with the software package ASPEN (Martin 2007). The time resolution is one observation every half second. This gives a vertical resolution of 5–6 m close to the surface and around 50 m at about 7-km height. After quality control several observations in each sounding are often discarded. This mostly affects the wind observations, which after quality control typically have more data gaps than the observations of temperature and humidity.

APPENDIX B: DATA MANAGEMENT. In Norway, IPY data management is organized through the national project DOKIPY (www.dokipy.no/), which is a distributed data management system with three nodes and is connected to the international IPY Data and Information Service (www.ipydis.org/). Each node is located at a governmental agency with a long-term commitment. The three nodes currently

TABLE 2. An overview of the technical specifications of the two lidar systems onboard the DLR Falcon aircraft. See Appendix A and references therein for more details.

	DIAL	Wind lidar
Transmitter type	Optical parametric oscillator (OPO) with a Nd:YAG laser	Thulium-doped $\text{Lu}_3\text{Al}_5\text{O}_{12}$ (Tm:LuAG) laser
Wavelength (nm)	532, 935 ($4\times$), 1,064	2,022
Pulse energy (mJ)	40	1.5
Pulse repetition frequency (Hz)	200 (4×50)	500
Average power (W)	8	0.75
Detection principle	Avalanche photodiode (APD)	PIN diode
Telescope diameter (cm)	48	10
Horizontal resolution (km)	0.15–0.5	0.15–40
Vertical resolution (km)	0.15–0.5	0.1
Absolute accuracy	Better than 10% (except for specific humidities $<$ a few ppb)	up to 0.1 m s^{-1}

contributing to DOKIPY are the Norwegian Meteorological Institute, the Institute of Marine Research, and the Norwegian Polar Institute. Between these nodes, metadata describing the IPY datasets managed by each node are exchanged on a daily basis. Furthermore, metadata are validated subsequent to a weekly harvest by the IPY portal at the National Aeronautics and Space Administration (NASA)'s Global Change Master Directory (GCMD). Through this exchange of metadata, IPY datasets managed through the DOKIPY system are directly linked to the central IPY metadata repository. All exchange of metadata both internally between the nodes and externally toward GCMD is done using the IPY metadata profile (<http://ipydis.org/data/metadata.html>), which is closely linked to the GCMD Directory Interchange Format (DIF) over the exchange protocol Open Archive Initiative Protocol for Metadata Harvesting (OAI-PMH; see www.openarchives.org/).

The DOKIPY node operated by the Norwegian Meteorological Institute (<http://dokipy.met.no/>) is used by IPY-THORPEX. Within this node data submitted must be formatted as NetCDF following the Climate and Forecast (CF; see <http://cf-pcmdi.llnl.gov/>) convention. This approach ensures that data collected are documented both at the discovery and use level. The CF convention ensures that NetCDF files are structured and essentially self-explaining for any user accessing the data. By adding global attributes supporting the discovery level metadata, the DOKIPY datasets hosted by the Norwegian Meteorological Institute are fully self-explanatory, containing information on who performed the measurement, when the measurement took place, what parameters were measured, what their units are, etc. An advantage of using NetCDF is that data can be made available online using a Thematic Realtime Environmental Distributed Data Services (THREDDS) data server (www.unidata.ucar.edu/projects/THREDDS/). Concerning long-term preservation, the data collected by IPY-THORPEX are entered into the long-term preservation archive maintained by the Norwegian Meteorological Institute upon submission in the appropriate form by the scientists. Upon submission, metadata are extracted and both metadata and data are checked for conformance with the file format specification. Properly documented and formatted datasets are facilitated for long-term stewardship.

As IPY ends, dedicated data management portals supporting IPY projects will eventually be closed. However, new data management frameworks are approaching. Key words for these are interoperability, distributed, and global. The World Meteorological

Organization (WMO) is establishing the WMO Information System (WIS; see www.wmo.int/pages/themes/wis/index_en.html), and the Norwegian Meteorological Institute has proposed to host an Arctic Data Centre within the WIS framework. All relevant datasets managed will be exposed through this and other portals that the Norwegian Meteorological Institute hosts. The intention is to keep datasets available online, but at some time in the future offline access to data may be necessary.

REFERENCES

- Aspelien, T., T. Iversen, J. B. Bremnes, and I.-L. Frogner, 2011: Short-range probabilistic forecasts from the Norwegian limited-area EPS: Long-term validation and a polar low study. *Tellus*, **63A**, 564–584.
- Barstad, I., and M. Adakudlu, 2011: Observation and modelling of gap flow and wake formation on Svalbard. *Quart. J. Roy. Meteor. Soc.*, doi:10.1002/qj.782, in press.
- , and Coauthors, 2008: The main observational campaign of the IPY/THORPEX-Norway project. Bjerknes Centre for Climate Research Rep. R29, 33 pp. [Available online at <http://folk.uib.no/ngfib/R29.pdf>.]
- Bishop, C. H., B. J. Etherton, and S. J. Majumdar, 2001: Adaptive sampling with the ensemble transform Kalman filter. Part I: Theoretical aspects. *Mon. Wea. Rev.*, **129**, 420–436.
- Blechschmidt, A.-M., H. Bakan, and H. Graßl, 2009: Large-scale atmospheric circulation patterns during polar low events over the Nordic Seas. *J. Geophys. Res.*, **114**, D06115, doi:10.1029/2008JD010865.
- Bracegirdle, T. J., and S. L. Gray, 2008: An objective climatology of the dynamical forcing of polar lows in the Nordic Seas. *Int. J. Climatol.*, **28**, 1903–1919, doi:10.1002/joc.1686.
- , and E. W. Kolstad, 2010: Climatology and variability of Southern Hemisphere marine cold-air outbreaks. *Tellus*, **62A**, 202–208.
- Brümmer, B., G. Müller, and G. Noer, 2009: A polar low pair over the Norwegian Sea. *Mon. Wea. Rev.*, **137**, 2559–2575.
- Buizza, R., and A. Montani, 1999: Targeting observations using singular vectors. *J. Atmos. Sci.*, **56**, 2965–2985.
- Cardinali, C., 2009: Monitoring the observation impact on the short-range forecast. *Quart. J. Roy. Meteor. Soc.*, **135**, 239–250.
- Carlson, D., T. E. Nordeng, and J. E. Kristjánsson, 2009: Advancing weather, ice and environmental predictions in the polar regions: An IPY legacy. WMO CAS Vision Paper on IPY, 5 pp. [Available online

- at www.wmo.int/pages/prog/arep/cas/documents/CAS_15Agendaitem8_4.pdf.]
- Collard, A. D., 2007: Selection of IASI channels for use in numerical weather prediction. *Quart. J. Roy. Meteor. Soc.*, **133**, 1977–1991.
- , and S. B. Healy, 2003: The combined impact of future space-based atmospheric sounding instruments on numerical weather-prediction analysis fields: A simulation study. *Quart. J. Roy. Meteor. Soc.*, **129**, 2741–2760.
- Douglas, M. W., L. S. Fedor, and M. A. Shapiro, 1991: Polar low structure over the northern Gulf of Alaska based on research aircraft observations. *Mon. Wea. Rev.*, **119**, 32–54.
- , M. A. Shapiro, L. S. Fedor, and L. Saukkonen, 1995: Research aircraft observations of a polar low at the east Greenland ice edge. *Mon. Wea. Rev.*, **123**, 5–15.
- Drüe, C., and G. Heinemann, 2001: Airborne investigation of arctic boundary-layer fronts over the marginal ice zone of the Davis Strait. *Bound.-Layer Meteor.*, **101**, 261–292.
- Duncan, C. N., 1977: A numerical investigation of polar lows. *Quart. J. Roy. Meteor. Soc.*, **103**, 255–267.
- Emanuel, K. A., and R. Rotunno, 1989: Polar lows as arctic hurricanes. *Tellus*, **41**, 1–17.
- Føre, I., J. E. Kristjánsson, Ø. Saetra, Ø. Breivik, B. Røsting, and M. Shapiro, 2011b: The full life cycle of a polar low over the Norwegian Sea observed by three research aircraft flights. *Quart. J. Roy. Meteor. Soc.*, doi:10.1002/qj.825, in press.
- Frogner, I.-L., and T. Iversen, 2001: Targeted ensemble prediction for Northern Europe and parts of the North Atlantic Ocean. *Tellus*, **53A**, 35–55.
- , and —, 2002: High-resolution limited-area ensemble predictions based on low-resolution targeted singular vectors. *Quart. J. Roy. Meteor. Soc.*, **128**, 1321–1341.
- , H. Haakenstad, and T. Iversen, 2006: Limited-area ensemble predictions at the Norwegian Meteorological Institute. *Quart. J. Roy. Meteor. Soc.*, **132**, 2785–2808.
- Gaberšek, S., and D. R. Durran, 2004: Gap flows through idealized topography. Part I: Forcing by large-scale winds in the nonrotating limit. *J. Atmos. Sci.*, **61**, 2846–2862.
- Grønås, S., and N. G. Kvamstø, 1995: Numerical simulations of the synoptic conditions and development of arctic outbreak polar lows. *Tellus*, **47A**, 797–814.
- , and P. Skeie, 1999: A case study of strong winds at an arctic front. *Tellus*, **51A**, 865–879.
- , A. Foss, and M. Lystad, 1987: Numerical simulations of polar lows in the Norwegian Sea. *Tellus*, **39A**, 334–353.
- Hanesiak, J., and Coauthors, 2010: Storm studies in the arctic (STAR). *Bull. Amer. Meteor. Soc.*, **91**, 47–68.
- Hilton, F., N. C. Atkinson, S. J. English, and J. R. Eyre, 2009: Assimilation of IASI at the Met Office and assessment of its impact through observing system experiments. *Quart. J. Roy. Meteor. Soc.*, **135**, 495–505.
- Holton, J. R., 2004: *An Introduction to Dynamic Meteorology*. 4th ed. Academic Press, 535 pp.
- Hoskins, B. J., M. E. McIntyre, and A. W. Robertson, 1985: On the significance of isentropic potential vorticity maps. *Quart. J. Roy. Meteor. Soc.*, **111**, 877–946.
- Irvine, E. A., S. L. Gray, and J. Methven, 2011: Targeted observations of a polar low in the Norwegian Sea. *Quart. J. Roy. Meteor. Soc.*, doi:10.1002/qj.914, in press.
- Kiemle, C., and Coauthors, 2007: Latent heat flux profiles from collocated airborne water vapor and wind lidars during IHOP_2002. *J. Atmos. Oceanic Technol.*, **24**, 627–639.
- Kolstad, E. W., and T. J. Bracegirdle, 2008: Marine cold air outbreaks in the future: An assessment of IPCC AR4 model results for the Northern Hemisphere. *Climate Dyn.*, **30**, 871–885.
- , —, and I. A. Seierstad, 2009: Marine cold-air outbreaks in the North Atlantic: Temporal distribution and associations with large-scale atmospheric circulation. *Climate Dyn.*, **33**, 187–197.
- Langland, R. H., 2005: Issues in targeted observing. *Quart. J. Roy. Meteor. Soc.*, **131**, 3409–3425.
- Linders, T., and Ø. Saetra, 2010: Can CAPE maintain polar lows? *J. Atmos. Sci.*, **67**, 2559–2571.
- Mailhot, J., D. Hanley, B. Bilodeau, and O. Hertzman, 1996: A numerical case study of a polar low in the Labrador Sea. *Tellus*, **48A**, 383–402.
- Mansfield, D. A., 1974: Polar lows: The development of baroclinic disturbances in cold air outbreaks. *Quart. J. Roy. Meteor. Soc.*, **100**, 541–554.
- Martin, C., 2007: *The ASPEN User Manual*. UCAR, 56 pp. [Available online at www.eol.ucar.edu/data/software/aspen/Aspen%20Manual.pdf.]
- Mayer, S., A. Sandvik, M. Jonassen, and J. Reuder, 2011: Atmospheric profiling with the UAS SUMO: A new perspective for the evaluation of fine-scale atmospheric models. *Meteor. Atmos. Phys.*, doi:10.1007/s00703-010-0063-2, in press.
- McInnes, H., J. Kristiansen, J. E. Kristjánsson, and H. Schyberg, 2011: The role of horizontal resolution for polar low simulations. *Quart. J. Roy. Meteor. Soc.*, doi:10.1002/qj.849, in press.
- Meischner, P., R. Baumann, H. Höller, and T. Jank, 2001: Eddy dissipation rates in thunderstorms estimated by

- Doppler radar in relation to aircraft in situ measurements. *J. Atmos. Oceanic Technol.*, **18**, 1609–1627.
- Montgomery, M. T., and B. F. Farrell, 1992: Polar low dynamics. *J. Atmos. Sci.*, **49**, 2484–2505.
- Noer, G., and M. Ovhed, 2003: Forecasting of polar lows in the Norwegian and the Barents Sea. *Proc. Ninth Meeting of the EGS Polar Lows Working Group*, Cambridge, United Kingdom, European Geophysical Society. [Available online at http://www2.meteo.uni-bonn.de/mitarbeiter/alte_seiten/GHeinemann/eplwg/newl03/noer/wplwg-2003-forecasting_polar_lows.html.]
- Nordeng, T. E., G. Brunet, and J. Caughey, 2007: Improvements of weather forecasts in polar regions. *WMO Bull.*, **56**, 250–257.
- Ólafsson, H., and H. Ágústsson, 2007: The Freynesnæs downslope windstorm. *Meteor. Z.*, **16**, 123–130.
- Plant, R. S., G. C. Gray, and S. L. Gray, 2003: On a threefold classification of extratropical cyclogenesis. *Quart. J. Roy. Meteor. Soc.*, **129**, 2989–3012.
- Randriamampianina, R., and A. Storto, 2008a: Aladin-HARMONIE/Norway and its assimilation system—The implementation phase. *HIRLAM Newsletter*, Vol. 54, 20–30. [Available online at http://hirlam.org/index.php?option=com_docman&task=doc_download&Itemid=70&gid=128.]
- , and —, 2008b: Monitoring the use of IASI data in a limited area data assimilation system. *Proc. 16th Int. TOVS Study Conf.*, Angra Dos Reis, Brazil, International TOVS Working Group. [Available online at www.eumetsat.int/groups/cps/documents/document/pdf_conf_p_s12_55_storto_p.pdf.]
- , T. Iversen, and A. Storto, 2011: Exploring the assimilation of IASI radiances in forecasting polar lows. *Quart. J. Roy. Meteor. Soc.*, doi:10.1002/qj.838, in press.
- Rasmussen, E., 1979: The polar low as an extratropical CISK disturbance. *Quart. J. Roy. Meteor. Soc.*, **105**, 541–549.
- , 1981: An investigation of a polar low with a spiral cloud structure. *J. Atmos. Sci.*, **38**, 1785–1792.
- , and J. Turner, Eds., 2003: *Polar Lows: Mesoscale Weather Systems in the Polar Regions*. Cambridge University Press, 612 pp.
- , —, K. Ninoyima, and I. A. Renfrew, 2003: Observational studies. *Polar Lows: Mesoscale Weather Systems in the Polar Regions*, E. Rasmussen and J. Turner, Eds., Cambridge University Press, 150–285.
- Renfrew, I. A., G. W. K. Moore, and A. A. Clerk, 1997: Binary interactions between polar lows. *Tellus*, **49A**, 577–594.
- , and Coauthors, 2008: The Greenland flow distortion experiment. *Bull. Amer. Meteor. Soc.*, **89**, 1307–1324.
- , S. D. Outten, and G. W. K. Moore, 2009: An easterly tip jet off Cape Farewell, Greenland. I: Aircraft observations. *Quart. J. Roy. Meteor. Soc.*, **135**, 1919–1933.
- Reuder, J., P. Brisset, M. Jonassen, M. Müller, and S. Mayer, 2009: The small unmanned meteorological observer SUMO: A new tool for atmospheric boundary layer research. *Meteor. Z.*, **18**, 141–147.
- Sandvik, A. D., and B. R. Furevik, 2002: Case study of a coastal jet at Spitsbergen—Comparison of SAR- and model-estimated wind. *Mon. Wea. Rev.*, **130**, 1040–1051.
- Shapiro, M. A., L. S. Fedor, and T. Hampel, 1987: Research aircraft measurements of a polar low over the Norwegian Sea. *Tellus*, **39A**, 272–306.
- , T. Hampel, and L. S. Fedor, 1989: Research aircraft observations of an arctic front over the Barents Sea. *Polar and Arctic Lows*, P. F. Twitchell, E. Rasmussen, and K. L. Davidson, Eds., Deepak, 279–289.
- Skeie, P., and S. Grønås, 2000: Strongly stratified easterly flows across Spitsbergen. *Tellus*, **52A**, 473–486.
- Smith, R. B., 2002: Stratified airflow over mountains. *Environmental Stratified Flows*, R. Grimshaw, Ed., Kluwer, 119–159.
- Tjernström, M., and Coauthors, 2005: Modelling the arctic boundary layer: An evaluation of six ARCMIP regional-scale models using data from the SHEBA project. *Bound.-Layer Meteor.*, **117**, 337–381.
- Wagner, J. S., A. Gohm, A. Dörnbrack, and A. Schäfler, 2011: The mesoscale structure of a mature polar low: Airborne lidar measurements and simulations. *Quart. J. Roy. Meteor. Soc.*, **137**, 1516–1531.
- Weissmann, M., R. Busen, A. Dörnbrack, S. Rahm, and O. Reitebuch, 2005: Targeted observations with an airborne wind lidar. *J. Atmos. Oceanic Technol.*, **22**, 1706–1719.
- Wirth, W., A. Fix, P. Mahnke, H. Schwartzer, F. Schrandt, and G. Ehret, 2009: The airborne multi-wavelength water vapor differential absorption lidar WALES: System design and performance. *Appl. Phys.*, **96B**, 201–213.
- Yano, J.-I., and J.-F. Geleyn, 2010: Challenges for a new generation of regional forecast models. *Eos, Trans. Amer. Geophys. Union*, **91**, 232.